Journal of
METAMORPHIC GEOLOGY

J. metamorphic Geol., 2013, **31,** 729–753 doi:10.1111/jmg.12042

A window into the Early to mid-Cretaceous infrastructure of the Yukon-Tanana terrane recorded in multi-stage garnet of west-central Yukon, Canada

R. D. STAPLES,[1] H. D. GIBSON,[1] R. G. BERMAN,[2] J. J. RYAN[3] AND M. COLPRON[4]
[1]*Department of Earth Sciences, Simon Fraser University, Burnaby, BC, V5A 1S6, Canada (rdstaple@sfu.ca)*
[2]*Geological Survey of Canada, Ottawa, ON, K1A 0E9, Canada*
[3]*Geological Survey of Canada, Vancouver, BC, V6B 5J3, Canada*
[4]*Yukon Geological Survey, Whitehorse, YK, Y1A 2C6, Canada*

ABSTRACT Amphibolite facies metasedimentary schists within the Yukon-Tanana terrane in the northern Canadian Cordillera reveal a two-stage, polymetamorphic garnet growth history. *In situ* U-Th-Pb Sensitive High Resolution Ion Microprobe dating of monazite provide timing constraints for the late stages of garnet growth, deformation and subsequent decompression. Distinct textural and chemical growth zoning domains, separated by a large chemical discontinuity, reveal two stages of garnet growth characterized in part by: (i) a syn-kinematic, inclusion-rich stage-1 garnet core; and (ii) an inclusion-poor, stage-2 garnet rim that crystallized with syn- to post-kinematic staurolite and kyanite. Phase equilibria modelling of garnet molar and compositional isopleths suggest stage-1 garnet growth initiated at ~600 °C, 8 kbar along a clockwise *P–T* path. Growth of the compositionally distinct, grossular-rich, pyrope-poor inner portion of the stage-2 overgrowth is interpreted to have initiated at higher pressure and/or lower temperature than the stage-1 core along a separate *P–T* loop, culminating at peak *P–T* conditions of ~650–680 °C and 9 kbar. Stage-2 metamorphism and the waning development of a composite transposition foliation (S_T) are dated at *c.* 118 Ma from monazite aligned parallel to S_T, and inclusions in syn- to post-S_T staurolite and kyanite. Slightly younger ages (*c.* 112 Ma) are obtained from Y-rich monazite that occurs within resorbed areas of both stage-1 and stage-2 garnet, together with retrograde staurolite and plagioclase. The younger ages obtained from these texturally and chemically distinct grains are interpreted, with the aid of phase equilibria calculations, to date the growth of monazite from the breakdown of garnet during decompression at *c.* 112 Ma. Evidence for continued near-isothermal decompression is provided by the presence of retrograde sillimanite, and cordierite after staurolite, which indicates decompression below ~4–5 kbar prior to cooling below ~550 °C. As most other parts of the Yukon-Tanana terrane were exhumed to upper crustal levels in the Early Jurassic, these data suggest this domain represents a tectonic window revealing a much younger, high-grade tectono-metamorphic core (infrastructure) within the northern Cordilleran orogen. This window may be akin to extensional core complexes identified in east-central Alaska and in the southeastern Canadian Cordillera.

Key words: *in situ* monazite geochronology; multi-stage garnet; *P–T–t* path; SHRIMP; Yukon-Tanana terrane.

INTRODUCTION

The geodynamic evolution of orogenic belts is dictated to a large extent by the rheology of the lithosphere, which in turn is controlled, in part, through a dynamic interplay between metamorphism and deformation. Understanding of the evolution of orogenic belts is, therefore, significantly aided by establishing the *P–T* conditions and style of deformation and metamorphism operating at various times and locations throughout an orogen. However, the diachronous and transitory nature of deformation and metamorphism across an orogen prohibits the correlation of metamorphic and deformational events solely on the basis of similarities in metamorphic mineral assemblage and structural style (Williams, 1985). This issue is compounded in the cores of orogenic belts, which may experience multiple episodes of deformation and metamorphism under nearly identical conditions.

The advent of *in situ* U-Pb monazite geochronology allows monazite to be dated in its petrological context with respect to metamorphic assemblages and fabric elements, thereby providing a greater level of confidence in establishing not only the age of metamorphism and the associated *P–T* conditions (Foster

et al., 2002, 2004; Gibson *et al.*, 2004) but also the timing of deformation fabrics (Williams & Jercinovic, 2002; Berman *et al.*, 2005, in press). Additionally, when coupled with analysis of garnet zoning patterns and phase diagram modelling, *in situ* U-Pb monazite dating can establish the timing of points along specific *P–T* paths (Berman *et al.*, 2007a, 2010, in press; Caddick *et al.*, 2007; Gaidies *et al.*, 2008). Applications of this method have also identified domains of contrasting *P–T–t* histories in areas previously considered to be part of a single tectono-metamorphic unit (Berman *et al.*, 2007a; Horváth *et al.*, 2010).

We apply similar techniques to amphibolite facies rocks of the Yukon-Tanana terrane, which occupies much of the metamorphic core of the orogen in the northern Canadian Cordillera and easternmost Alaska (Figs 1 & 2). Typical of the core zone of many orogenic belts, the Yukon-Tanana terrane rocks are poly-deformed and metamorphosed, with metamorphic and deformational events recorded in the Devono-Mississippian, Permo-Triassic, Jurassic and Cretaceous (see Berman *et al.*, 2007a for a review). Further complicating matters, mapping and *P–T-t–D* data (Berman *et al.*, 2007a) reveal that the style, pattern and grade of metamorphism and deformation was nearly identical in each of the Permo-Triassic, Jurassic and Cretaceous tectono-metamorphic events.

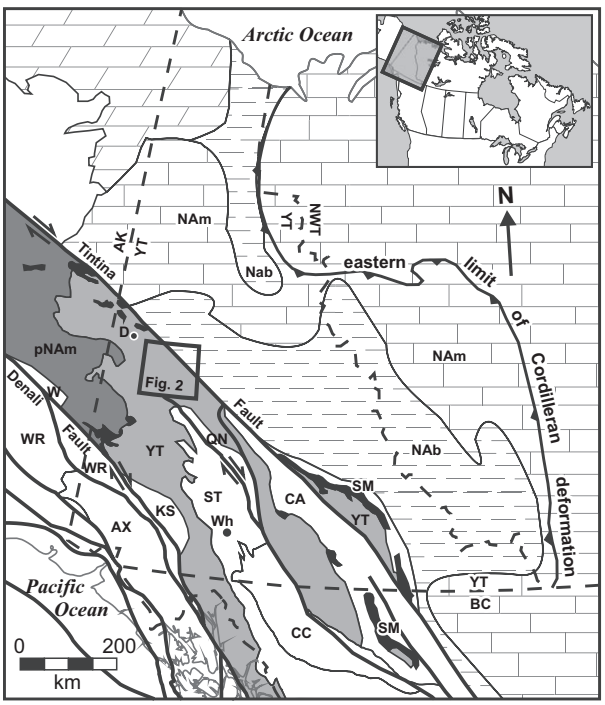

Figure 1. Simplified terrane map of the northern Canadian Cordillera showing location of Fig. 2, and the study area, within the northern portion of Yukon-Tanana terrane (modified from Colpron *et al.*, 2006). D, Dawson; Wh, Whitehorse. Lithotectonic terrane abbreviations: AX, Alexander; CA, Cassiar; CC, Cache Creek; KS, Kluane Schist; NAb, North American basinal strata; NAm, North American platformal strata; pNAm, parautochthonous North American continental margin; SM, Slide Mountain; ST, Stikinia; YT, Yukon-Tanana; W, Windy; WR, Wrangellia.

Difficulty in identifying distinct tectono-metamorphic domains within the Yukon-Tanana terrane, and deciphering discrete deformational and metamorphic events within an individual domain, are overcome herein by a detailed analysis of textural relationships and monazite and garnet chemistry. The timing of deformation and a segment of an individual *P–T* path are determined by *in situ* Sensitive High Resolution Ion Microprobe (SHRIMP) monazite geochronology, with monazite growth texturally and chemically linked to deformation fabrics as well as metamorphic porphyroblasts and their modelled *P–T* stability conditions. These data, together with the data of Berman *et al.* (2007a), elucidate a high-pressure Cretaceous tectono-metamorphic domain (Australia Mountain domain) that is distinct from an adjacent domain affected by Permo-Triassic and Early Jurassic events, and exhumed to upper crustal levels in the Early Jurassic. In this study, we better constrain the timing, nature and regional extent of Cretaceous metamorphism and decompression in west-central Yukon, and elucidate the structural-thermal architecture of the northern Cordilleran orogen in the Cretaceous.

GEOLOGICAL BACKGROUND

Northern Cordilleran orogen

The Yukon-Tanana terrane, together with Stikinia, Quesnellia and the oceanic Slide Mountain terrane, represent late Palaeozoic to Mesozoic arc and back-arc systems that lay outboard of the previously thinned, western ancestral North American margin (Colpron *et al.*, 2007). The timing and nature of accretion of the above terranes have been well documented in both the northern and the southern Canadian Cordillera (e.g. Monger *et al.*, 1982; Nelson *et al.*, 2006; Colpron *et al.*, 2007; Beranek & Mortensen, 2011). In the Mesozoic, the orogen grew as a consequence of protracted compression and crustal thickening during arc-continent collisions (e.g., Berman *et al.*, 2007a; Gibson *et al.*, 2008) as the North American craton moved westward, converging with its offshore subduction zone (Monger & Price, 2002). In the southern Canadian Cordillera, a significant body of geochronological data from the metamorphic core of the orogen has revealed that despite similarities in regional metamorphic grade and deformation patterns, both were strongly diachronous, younging systematically with increasing structural depth (Parrish, 1995). Rocks presently in the upper exposed structural levels were buried, heated and exhumed in the Jurassic (Murphy *et al.*, 1995; Colpron *et al.*, 1996; Gibson *et al.*, 2005), while structurally deeper

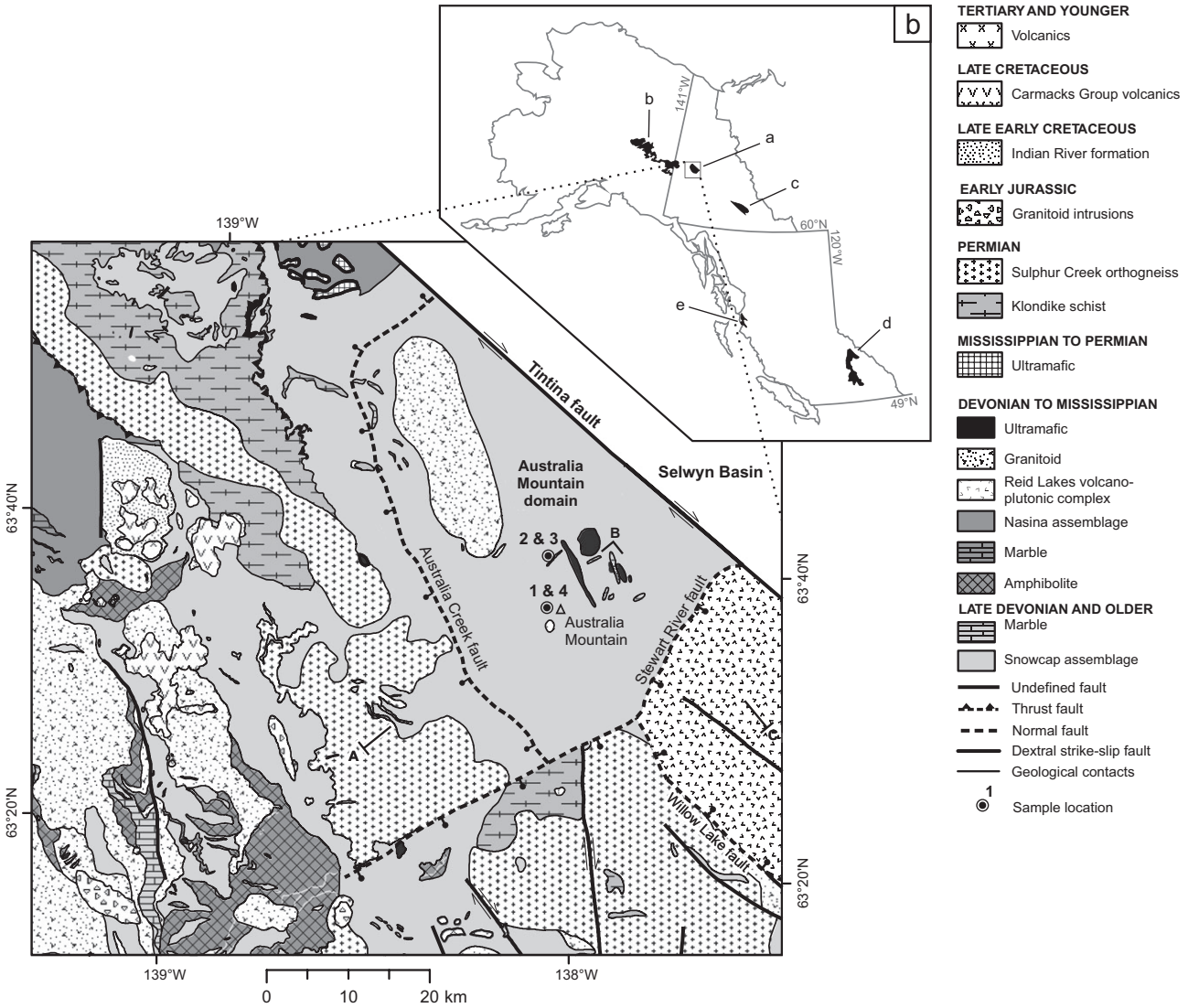

Figure 2. (a) Simplified geology for portions of Stewart River and McQuesten map areas showing the distribution of sample locations and the approximate boundary of the Early to mid-Cretaceous Australia Mountain metamorphic domain bounded by the Australia Creek, Stewart River and Tintina faults. Modified from Gordey & Ryan, 2005; Ryan *et al.*, 2010. (b) Map showing the distribution of rocks at mid- to lower crustal levels in the Early to mid-Cretaceous in the BC, Yukon and Alaskan Cordillera. Location abbreviations and references: a, this study and Berman *et al.* (2007a); b, east-central Alaska (Pavlis *et al.*, 1993; Dusel-Bacon *et al.*, 2002); c, Finlayson region (Murphy, 2004); d, Shushwap complex (Parrish, 1995; Crowley *et al.*, 2000; Gibson *et al.*, 2008); e, Prince Rupert area (Wolf *et al.*, 2010).

rocks were progressively buried and heated from at least Cretaceous to earliest Eocene (Carr, 1991; Parrish, 1995; Crowley & Parrish, 1999; Gibson *et al.*, 1999, 2005; Crowley *et al.*, 2000). The deepest structural levels within the core of the orogen, which includes autochthonous and parautochthonous North American crust, were largely exhumed by extensional shear zones in the early Eocene (Parrish *et al.*, 1988; Brown *et al.*, 2012), marking a shift to a transtensional tectonic setting.

The deformational and metamorphic history of the Yukon-Tanana terrane within the northern Cordillera differs from the southeastern Canadian Cordillera in that the main phase of metamorphism (amphibolite facies) and deformation appears to have occurred earlier, in the Late Permian to Early Triassic (Berman *et al.*, 2007a; Beranek & Mortensen, 2011). There was an ~8 kbar metamorphic overprint in the Early Jurassic before much of the metamorphic core of the northern Cordilleran orogen was rapidly exhumed in the Early to Middle Jurassic (Hansen *et al.*, 1991; Stevens *et al.*, 1993; Johnston *et al.*, 1996; Berman *et al.*, 2007a).

In east-central Alaska, the allochthonous Yukon-Tanana terrane is structurally underlain by a large area of metamorphic rocks interpreted by Dusel-Bacon

et al. (1995, 2002) to be part of the parautochthonous western continental margin of ancestral North America. In the pre-latest Triassic (>212 Ma), the uppermost structural levels of the allochthonous Yukon-Tanana terrane were affected by northeast-directed shear at 8–12 kbar (Dusel-Bacon *et al.*, 1995). By Early Jurassic (>188 Ma), both the lower structural levels of the allochthonous Yukon-Tanana terrane and the underlying parautochthonous rocks were deformed and metamorphosed at amphibolite facies conditions (7–12 kbar) during northwest-directed contraction and imbrication (Dusel-Bacon *et al.*, 1995). Early Jurassic $^{40}Ar/^{39}Ar$ cooling ages are interpreted by Hansen & Dusel-Bacon (1998), and Dusel-Bacon *et al.* (2002) to date the time of cooling of the upper plate following the aforementioned northwest-directed contraction that emplaced the allochthonous rocks of Yukon-Tanana terrane onto the parautochthonous continental margin. The lower plate was subsequently exhumed by southeast-directed crustal extension as recorded in *c.* 135–110 Ma $^{40}Ar/^{39}Ar$ cooling ages in parautochtonous continental margin rocks (Pavlis *et al.*, 1993; Hansen & Dusel-Bacon, 1998; Dusel-Bacon *et al.*, 2002). Exhumation of ductily deformed amphibolite facies rocks in the Early to mid-Cretaceous is also recorded <200 km to the east of the Cretaceous domain of east-central Alaska, in the Australia Mountain area of west-central Yukon. Although the timing of deformation and metamorphism appears to be older in the northern Cordillera, this diachroneity of tectonism, which may be a function of structural level and position within the orogenic wedge, suggests similarity with what is recorded in the southern Canadian Cordillera.

Australia mountain area

The Yukon-Tanana terrane has been dissected and offset ~430 km by the Tintina fault, an Eocene dextral strike-slip fault (Gabrielse *et al.*, 2006). The study area is located at Australia Mountain (Figs 1 & 2), immediately southwest of the Tintina fault, and is underlain by highly deformed psammite, semi-pelite and quartzite with lesser amounts of pelite, mafic volcanic and ultramafic rocks that have been metamorphosed to amphibolite facies. These rocks are widely accepted to be part of Yukon-Tanana terrane (eg. Mortensen, 1990; Gordey & Ryan, 2005; Ruks *et al.*, 2006; Berman *et al.*, 2007a), and we treat them as such here. However, as is elaborated in the discussion section, our data allow that the rocks could equally represent parautochthonous North American continental margin rocks that are structurally juxtaposed with Yukon-Tanana terrane similar to what is described by Dusel-Bacon *et al.* (2002) and Dusel-Bacon *et al.* (2006) in east-central Alaska. West and south of the Australia Mountain area are polydeformed and transposed amphibolite facies Palaeozoic rocks of the Yukon-Tanana terrane, which are intruded by weakly to undeformed plutons of Triassic, Jurassic, Cretaceous and Eocene age (Gordey & Ryan, 2005). These are overlain by Cretaceous and Paleocene volcanic and sedimentary rocks, and rare Quaternary basalt (Gordey & Ryan, 2005).

The main episode of deformation to the west and south of Australia Mountain, and generally considered representative for the Yukon-Tanana terrane in general, produced a regional transposition foliation that is interpreted by Berman *et al.* (2007a) and Beranek & Mortensen (2011) to be bracketed between *c.* 260 and 253 Ma. This constraint is based upon the ages obtained from the strongly foliated Sulphur Creek orthogneiss (*c.* 260 Ma), as well as the undeformed Jim Creek pluton (253 Ma), which cuts across the transposition foliation in the Devono-Mississippian Nasina assemblage (Beranek & Mortensen, 2011). A *c.* 239 Ma monazite included within garnet was interpreted by Berman *et al.* (2007a) to constrain the latter stages of a Late Permian to Middle Triassic tectonometamorphic event that was initiated at low pressure and culminated with the growth of garnet at ~9 kbar and 600 °C. A subsequent episode of metamorphism is recorded in *c.* 195–187 Ma monazite inclusions within garnet and kyanite porphyroblasts, which are interpreted by Berman *et al.* (2007a) to date an Early Jurassic metamorphic event with peak conditions of ~8 kbar and 600 °C. Unlike the Permo-Triassic event, this Early Jurassic metamorphism was not accompanied by significant fabric development, rather Berman *et al.* (2007a) suggested the strain was partitioned heterogeneously into regional high-strain zones. West of Australia Mountain, amphibolite facies rocks of the Snowcap assemblage and structurally lower level Permian rocks at greenschist facies were interpreted by Mackenzie & Craw (2012) to be thrust imbricated along localized ductile and brittle Jurassic shear zones that were active at greenschist facies conditions.

The amphibolite facies rocks west and south of the Australia Mountain area yield Early to Middle Jurassic K-Ar cooling ages (Hunt & Roddick, 1992), interpreted to record widespread exhumation and cooling below ~300 °C. In contrast, strongly deformed, amphibolite facies rocks at Australia Mountain are juxtaposed to the southeast against essentially undeformed and unmetamorphosed rocks of the Mississippian Reid Lakes volcano-plutonic complex (Colpron & Ryan, 2010). The preservation of Mississippian $^{40}Ar/^{39}Ar$ cooling ages throughout the Reid Lakes complex (Knight *et al.*, 2013) indicates it was not significantly buried or heated during the Permian and Jurassic tectonometamorphic events. This is also consistent with the lack of observed deformation and metamorphism within the complex. The boundary between the Australia Mountain domain and these adjacent distinct domains are inferred as normal faults, herein named the Australia Creek and Stewart River faults (Fig. 2).

At Australia Mountain, the rocks are characterized by a strong, penetrative foliation that is parallel to the axial planes of tight to isoclinal folds. Primary compositional layering in metasedimentary rocks and a pre-existing foliation can be traced around the closures of these tight to isoclinal folds indicating that the folds are at least F_2 structures. The presence of rootless intrafolial isoclinal folds suggests this foliation is likely a composite transposition foliation in the sense of Williams (1983) and Tobisch & Paterson (1988). Following Williams & Compagnoni (1983), we have notated this composite transposition foliation as S_T. S_T has in turn been deformed by at least two later episodes of folding, herein denoted F_{T+1} and F_{T+2}. The F_{T+1} folds are subhorizontal to gently plunging, steeply to moderately inclined, tight asymmetric chevron folds with more open parasitic crenulations. The F_{T+1} folds lack an axial planar foliation, and show no signs of development of a crenulation cleavage. The latest phase of folding, F_{T+2}, consists of subhorizontal, upright gentle to open folds. The metamorphic grade, style, orientation and pattern of successive phases of deformation within this Cretaceous domain are strikingly similar to those found in the surrounding Permo-Triassic and Jurassic metamorphic domain (Ryan *et al.*, 2003). Through the application of high resolution *in situ* U-Pb monazite dating, linked to the *P–T* history and deformation fabrics, we herein shed light on the unique Early to mid-Cretaceous metamorphic, deformational and exhumation history for this portion of the Yukon-Tanana terrane.

PETROLOGICAL METHODS

Thermobarometry

Mineral compositions were quantitatively analyzed using a fully automated CAMECA SX-50 instrument, operating in wavelength-dispersion mode with the following operating conditions: excitation voltage, 15 kV; beam current, 20 nA (10 nA for mica); peak count time, 20 s (40 s for F, Cl); background count-time, 10 s (20 s for F, Cl); spot diameter, 5 μm. Quantitative data were obtained for garnet, biotite, plagioclase and muscovite (Table 1). Temperatures and pressures were calculated using the winTWQ program (version 2.32; Berman, 2007), which uses internally consistent thermodynamic data for end-members and mixing properties to calculate the average *P–T* values from the intersections among the following independent set of equilibria (mineral abbreviations after Kretz, 1983):

$$\mathrm{Alm} + \mathrm{Phl} = \mathrm{Pyp} + \mathrm{Ann} \quad (1)$$

$$\mathrm{Grs} + 2\mathrm{Ky} + \mathrm{Qtz} = 3\mathrm{An} \quad (2)$$

$$3\mathrm{East} + 2\mathrm{Grs} + \mathrm{Pyp} + 6\mathrm{Qtz} = 3\mathrm{Phl} + 6\mathrm{An} \quad (3)$$

$$\mathrm{Alm} + \mathrm{Grs} + \mathrm{Ms} = 3\mathrm{An} + \mathrm{Ann} \quad (4)$$

The winTWQ software incorporates solution solid solution models for garnet and biotite (Berman, 2007), as well as for plagioclase (Fuhrman & Lindsley, 1988) and muscovite (Chatterjee & Froese, 1975). For samples 1 and 2 with sodic-rich plagioclase, the aluminium-avoidance plagioclase model of Aranovich (1991) was used. This model yields lower pressures that are generally more consistent with independent estimates (Aranovich, 1991). Absolute errors of thermobarometric data are considered to be $\sim \pm 50$ °C and 1 kbar (Berman, 1991), with appreciably smaller errors associated with relative differences between samples.

Phase diagram calculations

Isochemical phase diagram sections were calculated in the system MnO-Na_2O–CaO–K_2O–FeO–MgO–Al_2O_3–SiO_2–H_2O–TiO_2-Fe_2O_3 with the program Domino (De Capitani & Brown, 1987; De Capitani & Petrakakis, 2010; http://titan.minpet.unibas.ch/minpet/theriak/theruser.html, version 01.08.09), and the internally consistent thermodynamic data set of Holland & Powell (1998); data set tcds55, created on 22 November 2003. Activity-composition models were used for the following phases: muscovite, excluding the margarite component (Coggon & Holland, 2002), feldspar (Holland & Powell, 2003), garnet and biotite (White *et al.*, 2007), ilmenite-hematite and magnetite-ulvospinel (White *et al.*, 2000), chlorite, cordierite, chloritoid, staurolite and epidote (Holland & Powell, 1998). All other phases were treated as pure. Garnet, biotite, staurolite, chloritoid, chlorite and cordierite were extended to the Mn-bearing system as outlined in Tinkham *et al.* (2001). A pure H_2O fluid was considered in excess in all calculations. Additionally, excess SiO_2 was added for sample 1 calculations. Silicate melt was not included in the calculations. Bulk rock compositions (Table 2a) were determined by whole-rock XRF analysis from thin section offcuts. A nominal amount of Fe_2O_3 (0.01 mol.% Fe_2O_3) was added to the system to be consistent with the garnet and biotite solution models of White *et al.* (2007), which incorporate Fe_2O_3. A small amount of Fe_2O_3 is consistent with ilmenite as the only Fe-bearing oxide, suggesting these rocks are fairly reduced.

The effective bulk composition of a rock changes with *P–T* as material is progressively fractionated within the cores of mineral grains with slow intracrystalline diffusion rates (Stüwe, 1997). Evidence for such slow diffusivity, and a changing effective bulk composition, is seen in the preservation of zoned minerals, in particular garnet. Phase diagrams calculated from the bulk whole-rock analysis are therefore only strictly correct at the *P–T* conditions during the

Table 1. Microprobe analyses used in *P–T* calculations.

	Sample 1 (09RS190A1)			Sample 2 (09RS172B1)				Sample 3 (09RS171A1)				
Mineral	Grt-2			Grt-1	Grt-2			Grt-1	Grt-2			
Position	Rim	Pl	Bt	Core	Rim	Pl	Bt	Core	Rim	Pl	Bt	Ms
wt% oxides												
SiO_2	37.13	63.13	37.32	36.74	36.52	61.61	35.50	37.03	36.90	61.22	35.30	44.76
TiO_2	0.00	n.d	1.56	0.06	0.03	n.d.	1.84	0.07	0.00	n.d.	2.26	0.37
Al_2O_3	21.94	22.59	17.94	21.20	21.46	24.08	18.61	21.43	21.68	24.90	20.14	35.82
FeO*	32.79	0.35	17.40	35.72	34.46	0.10	20.53	33.31	30.75	0.18	21.21	1.17
MgO	4.93	0.00	12.50	2.53	3.20	0.00	9.35	1.23	2.63	0.00	7.72	0.48
MnO	0.55	0.02	0.05	1.02	0.50	0.02	0.03	2.08	4.35	0.00	0.25	0.00
CaO	2.18	3.68	0.00	2.28	3.59	5.36	0.00	5.53	3.93	6.09	0.00	0.04
Na_2O	0.00	9.21	0.45	0.02	0.01	8.42	0.27	0.00	0.03	7.84	0.30	0.87
K_2O	n.d.	0.11	8.61	n.d.	n.d.	0.09	8.99	n.d.	n.d.	0.19	9.02	9.83
Total	99.53	99.09	96.32	99.58	99.81	99.67	95.70	100.72	100.28	100.42	96.57	93.69
Cations												
Oxygen	12	8	11	12	12	8	11	12	12	8	11	11
Si	2.96	2.82	2.78	2.98	2.94	2.74	2.72	2.97	2.96	2.72	2.68	3.03
Ti	0.00	n.d.	0.09	0.00	0.00	n.d.	0.11	0.00	0.00	n.d.	0.13	0.02
Al	2.06	1.19	1.57	2.03	2.04	1.26	1.68	2.03	2.05	1.30	1.80	2.86
Fe[a]	2.18	0.01	1.08	2.42	2.32	0.00	1.31	2.24	2.06	0.01	1.34	0.07
Mn	0.04	0.00	0.00	0.07	0.03	0.00	0.00	0.14	0.30	0.00	0.02	0.00
Mg	0.59	0.00	1.39	0.31	0.38	0.00	1.07	0.15	0.31	0.00	0.87	0.05
Ca	0.19	0.18	0.00	0.20	0.31	0.26	0.00	0.48	0.34	0.29	0.00	0.00
Na	0.00	0.80	0.06	0.00	0.00	0.73	0.04	0	0.00	0.67	0.04	0.11
K	n.d.	0.01	0.82	n.d.	n.d.	0.01	0.88	n.d.	n.d.	0.01	0.87	0.85
Fe/(Fe + Mg)	0.79		0.44	0.89	0.86		0.55	0.94	0.87		0.61	
X_{Alm}	0.73			0.81	0.76			0.75	0.69			
X_{Pyp}	0.20			0.10	0.13			0.05	0.10			
X_{Grs}	0.06			0.07	0.10			0.16	0.11			
X_{Sps}	0.01			0.02	0.01			0.05	0.10			
X_{An}		0.26				0.26				0.30		

[a]All Fe assumed to be Fe^{2+}.

Table 2. (a) Representative bulk-rock geochemical analyses (wt %). (b) Normalized effective bulk composition for the growth of stage-2 garnet (wt%).

Sample	1	2	3
(a)			
SiO_2	51.20	43.40	42.80
TiO_2	0.90	1.30	1.06
Al_2O_3	21.40	30.50	23.00
FeO[a]	10.15	11.25	16.90
MgO	3.01	3.23	2.38
MnO	0.12	0.10	0.92
CaO	2.37	1.37	4.00
Na_2O	5.72	2.44	2.20
K_2O	1.54	1.92	2.89
LOI	0.40	1.97	0.40
Total	96.81	97.48	96.55
(b)			
SiO_2	54.43	44.97	45.53
TiO_2	1.00	1.38	1.21
Al_2O_3	22.34	31.72	24.31
FeO[a]	8.37	10.50	15.40
MgO	2.83	3.29	2.51
MnO	0.03	0.07	0.89
CaO	2.48	1.35	3.90
Na_2O	6.36	2.59	2.51
K_2O	1.71	2.04	3.29
LOI	0.44	2.09	0.46
Total	100.00	100.00	100.00
Grt-1 mode[a]	7	3.4	9

Compositions in Table 2b represent the effective bulk composition during growth of stage-2 garnet overgrowths (Grt-2) following the fractionation of components into the core of stage-1 garnet (Grt-1). The effective bulk compositions were calculated by subtracting the average composition of stage-1 garnet (Grt-1) from the whole-rock XRF analysis, with the modal amount of Grt-1 estimated from image analysis of thin sections.

[a]Modal amount of Grt-1 subracted in the calculation of the effective bulk composition.

initial stage of garnet growth. Phase diagrams and compositional isopleths calculated from the whole-rock analysis were therefore used to estimate the prograde *P–T* path during the early stages of garnet growth. Isochemical phase diagrams, which are more suitable for modelling peak and retrograde metamorphic conditions, were constructed from an effective bulk composition calculated by subtracting the average composition of stage-1 garnet from the whole-rock XRF analysis. Whole-rock analyses and calculated effective bulk compositions used in the construction of phase diagrams are listed in Table 2a,b. There is no evidence to suggest that the bulk composition was further modified by open system behaviour. For instance, the absence of evidence for partial melt suggests the bulk composition was not modified by melt loss. Furthermore, the mineralogical, chemical and textural features suggest the rock was not affected by fluid alteration following regional metamorphism.

Some discrepancy in *P–T* estimates can be expected to arise from the different thermodynamic data utilized in the phase equilibria modelling and thermobarometric calculations. Nonetheless, the win-TWQ program was utilized because its calibration of equilibrium (3), a useful barometer for the aluminosilicate- and muscovite-absent rocks, is based on experimental data directly constraining eastonite properties (Berman *et al.*, 2007b).

PETROGRAPHY AND MINERAL CHEMISTRY

Four samples from Australia Mountain were selected for thermobarometric and geochronological analysis. Metamorphic mineral assemblages and coordinates of the sample localities are provided in Table 3. The investigated samples are garnet-bearing psammitic and pelitic schists characterized by garnet porphyroblasts that typically show two distinct domains: a resorbed, inclusion-rich darker coloured core (Grt-1) and a lighter, inclusion-poor, euhedral overgrowth (Grt-2) (Fig. 3a,c–e). A penetrative foliation (S_T) is generally defined within psammitic schists by quartz ribbons, elongated plagioclase and micaceous-rich layers. In some pelitic schists, staurolite and kyanite porphyroblasts are consistently aligned parallel to S_T, and exhibit kinked, bent and sweeping extinction indicative of syn-kinematic growth with respect to S_T (Fig. 3b,f). However, in other semipelitic schists staurolite and kyanite have a weak preferred orientation and may, or may not, contain intracrystalline evidence for deformation. Many other staurolite and kyanite grains in this same rock are randomly oriented with homogenous extinction, showing no evidence of strain. Staurolite and kyanite growth in the Australia Mountain area is therefore interpreted as syn- to post-kinematic with respect to S_T.

Grt-1 occasionally contains a sigmoidal inclusion-trail (S_i) that in rare samples is continuous with the external transposition foliation (S_T) (Fig. 3a), suggestive of early growth under conditions of non-coaxial shearing. By contrast, Grt-2 has fewer primary inclusions, is typically subhedral to euhedral, and has well-developed crystal faces modified by late-stage resorption (Fig. 3c,d). Partial breakdown of Grt-2 rims to randomly oriented mats of biotite masks the relationship of the foliation to Grt-2. Where Grt-2 has not been resorbed, it is characterized by straight, euhedral crystal faces that appear to truncate S_T (Fig. 3c,d), indicative of post-kinematic growth.

The boundary between Grt-1 and -2 is consistently marked by a large chemical discontinuity in all samples (Fig. 4). Grt-1 generally has low Fe/(Fe + Mg) and grossular contents that both decrease rimward in some samples. The inner portion of Grt-2 generally has markedly higher grossular, and lower almandine and pyrope than Grt-1. Fe/(Fe + Mg) and spessartine decrease towards the outer rim, characteristic of prograde growth zoning (Tracy *et al.*, 1976; Spear *et al.*, 1990; Florence & Spear, 1993). A slight kick-up in spessartine and Fe/(Fe + Mg) at the outer 100 μm of Grt-2 adjacent to both plagioclase and biotite is attributed to retrograde garnet resorption (Kohn & Spear, 2000). Biotite grains immediately adjacent to garnet have the highest Fe/(Fe + Mg) values. Otherwise, biotite grains >300 μm from garnet are 0.05 to 0.07 lower in Fe/(Fe + Mg) and have very little compositional variation (<0.02). Matrix plagioclase has a variable composition, with the lowest anorthite contents (X_{An} = 0.17–0.20) consistently within the cores of matrix grains of all samples, and the highest anorthite content (X_{An} = 0.25–0.34) within the rims of matrix grains immediately adjacent to strongly resorbed portions of garnet (X_{An} = 0.30).

Sample 1

Sample 1 is an Ilm-St-Grt-Bt-Pl-Qtz-bearing psammitic schist. It shares the textural and chemical features described above, but shows additional complexities and a unique textural relationship with monazite that warrant more detailed description. Portions of Grt-1, the outer portion of Grt-2, as well as the interface between them have been partially replaced by plagioclase, fine-grained euhedral staurolite and Y-rich monazite (Fig. 3c,d), forming an island (Grt-1) and atoll (Grt-2) structure. Staurolite and monazite do not occur as inclusions in either Grt-1 or Grt-2. In addition to the garnet chemical zoning described above, it is noteworthy that garnet has the same composition at its interface with the replacement products, St-Pl-Mnz, at the Grt-1 rim, Grt-2 inner rim, and Grt-2 outer rim (Fig. 4). Skeletal staurolite also occurs within the matrix of sample 1 where it is aligned parallel to the relict foliation and is deflected around garnet (Fig. 3d). The pre- to syn-kinematic nature of this matrix staurolite, together with its resorbed/skeletal texture, suggests it is an earlier generation than the euhedral, retrograde

Table 3. Summary of thermobarometric and geochronological data.

Sample no.	Field no.	UTM (zone 7 NAD 83) Easting	Northing	Main assemblage	Stage-2 Grt rim peak thermobarometry P[a] (kbar)	T (°C)	Eq.[b]	Age[c] (Ma)	Interpretation
1	09RS190A1	642809	7056955	St-Grt-Bt-Pl-Qtz[d]	8.8	650	1, 3	120 ± 3	Prograde M2, syn- to post-S_T
					8	650	pd	112 ± 6	M2 decompression
2	09RS172B1	641621	7063232	Ky-St-Crd-Grt-Bt Qtz-Pl	8.9	650	1, 2, 3	118 ± 2	Prograde M2, syn- to post-S_T
3	09RS171A1	641101	7063420	Ms-Bt-Grt-Pl-Qtz	9–10	680	1, 3, 4	–	Prograde M2, syn- to post-S_T
4	09RS188A2	642122	7057171	Sil-Grt-Crd-St-Ky- Bt-Pl-Qtz	–	–	–	117 ± 1	Prograde M2, syn- to post-S_T

[a]Estimated uncertainties are ± 1 kbar and 50 °C (Berman, 1991).
[b]Equilibria used to derive listed *P–T* values (pd = phase diagram constraints.
[c]All ages determined by *in situ* SHRIMP analysis of monazite. All ages represent weighted mean $^{206}Pb/^{238}U$ ages (2 sigma errors) of texturally and chemically similar monazite grains discussed in text.
[d]Minerals listed from least to most abundant.

staurolite that occurs within resorbed portions of garnet.

Sample 2

Sample 2 is a weakly foliated Ilm-Ky-St-Crd-Grt-Bt-Qtz-Pl-bearing semipelitic schist. Staurolite and kyanite have both a weak preferred orientation with undulatory extinction and are also randomly oriented with homogenous extinction. Staurolite, and less commonly kyanite, is rimmed by cordierite that contains numerous inclusions of fine-grained biotite. Garnet porphyroblasts are <8.0 mm in diameter and commonly have an atoll texture characterized by a subhedral garnet atoll (Grt-2) surrounding an interior of quartz, biotite and plagioclase. Other garnet porphyroblasts are present which show no chemical indication of a multi-stage growth history. These porphyroblasts are interpreted as stage-2 garnet from their similarity in texture, composition and zoning pattern to stage-2 overgrowths.

Sample 3

Sample 3 is a garnet-rich Ilm-Ms-Bt-Grt-Pl-Qtz-bearing psammitic schist. A penetrative schistose foliation is defined at outcrop and hand sample scale by elongate feldspar grains, and aligned biotite and muscovite that are deflected around garnet porphyroblasts. At thin-section scale, mica is randomly oriented, possibly due to a late episode of static recrystallization that masks the foliation and its timing of development relative to garnet growth. However, the presence of quartz and plagioclase pressure shadows aligned parallel to the foliation on opposite sides of euhedral garnet porphyroblasts indicates that the latter stages of garnet growth were synchronous with deformation. Muscovite, which is present only in sample 3, has a slight phengitic content (Si pfu = 3.1–3.2), generally non-detectable Ca, and Na/(Na + K + Ca) values of 0.08–0.10.

Sample 4

Sample 4 is a Rt-Sil-Grt-Crd-St-Ky-Bt-Pl-Qtz-bearing metapelite. Garnet occurs as rare, small (<1 mm), heavily resorbed grains both in the matrix and as inclusions within kyanite. Garnet that occurs both in the matrix and included in kyanite is partly replaced by biotite and plagioclase. Staurolite and kyanite contain kinked and sweeping extinction and are consistently aligned parallel to S_T, indicative of syn-kinematic growth with respect to S_T (Fig. 3b,f). Trains of elongated rutile grains are aligned parallel to, and help define, the S_T foliation. Cordierite appears texturally late, forming replacement rims around staurolite, and to a lesser extent around kyanite, and occurs throughout the matrix with numerous inclusions of biotite. A small amount of fibrolitic sillimanite is present in small patches of radiating fibres (Fig. 3f).

PARAGENETIC INTERPRETATION OF TEXTURAL AND CHEMICAL RELATIONS IN GARNET

Sample 3 is the only sample which records pronounced chemical zoning of the inclusion-rich garnet core, with rimward decreasing X_{Sps}, X_{Grs} and Fe/(Fe + Mg), and increasing X_{Alm} and X_{Pyp} characteristic of prograde growth zoning produced along a clockwise *P–T* path (Tracy *et al.*, 1976; Spear *et al.*, 1990; Florence & Spear, 1993). However, the sharp compositional gradient/discontinuity between Grt-1 and Grt-2 (Fig. 4), with the latter characterized by an increase in Fe/(Fe + Mg) and a decrease in X_{Pyp}, does not conform to a *P–T* path of increasing temperature required for garnet growth (Figs 5 & 6). Rather, the sharp compositional gradient between Grt-1 and -2 is interpreted as a zone of incomplete diffusional re-equilibration that developed following growth of the chemically distinct garnet overgrowth (Grt-2). The arrangement of X_{Grs} isopleths for sample 2 (Fig. 5) suggests growth of the grossular-rich Grt-2 initiated at significantly higher pressure and/or lower temperature than Grt-1.

Within the core of Grt-2, the decreasing Fe/(Fe + Mg), X_{Sps} and X_{Grs} values away from the zone of diffusional re-equilibration towards the rim is interpreted as a growth zoning pattern similar to Grt-1, but one that developed during a subsequent metamorphic event. Enrichment of spessartine and Fe/(Fe + Mg) at the extreme Grt-2 rim, and Fe-enriched biotite immediately adjacent to resorbed portions of garnet, are features characteristic of

Figure 3. Photomicrographs of samples 1, 2 and 4. (a) Garnet porphyroblast of sample 1 consisting of: (i) a syn-kinematic garnet core (Grt-1), which hosts a sigmoidal inclusion trail (S_i) that is continuous with the external transposition foliation (S_T), and (ii) an inclusion-poor overgrowth (Grt-2) on the top and bottom of the porphyroblast. (b) Sample 4, hand sample with elongate syn-kinematic staurolite (St) and kyanite (Ky) porphyroblasts consistently aligned parallel to the transposition foliation (S_T). (c) Garnet porphyroblast from sample 1 consisting of an inclusion-rich core (Grt-1) surrounded by an annulus of euhedral staurolite and plagioclase, and an inclusion-poor garnet atoll (Grt-2). Both the garnet core and atoll from sample 1 are resorbed and replaced by staurolite and plagioclase. The microprobe traverse displayed in Fig. 4a is shown in blue. (d) Garnet core and atoll of sample 1 replaced by euhedral staurolite and plagioclase. Skeletal matrix staurolite aligned parallel to the transposition foliation (S_T) is deflected around the garnet porphyroblasts, and is interpreted as an earlier generation than that which replaced garnet. (e) Garnet porphyroblast from sample 2, which consists of an inclusion-rich garnet core (Grt-1), and, with the exception of ilmenite (black inclusion), a relatively inclusion-poor overgrowth (Grt-2). The blue line across garnet shows the location of the microprobe traverse displayed in Fig. 4b. (f) Syn-kinematic porphyroblasts of staurolite and kyanite aligned parallel to S_T in sample 4. Fibrolitic sillimanite (Sil) occurs as small radiating fibres. Note: All mineral abbreviations used in figures are after Kretz (1983).

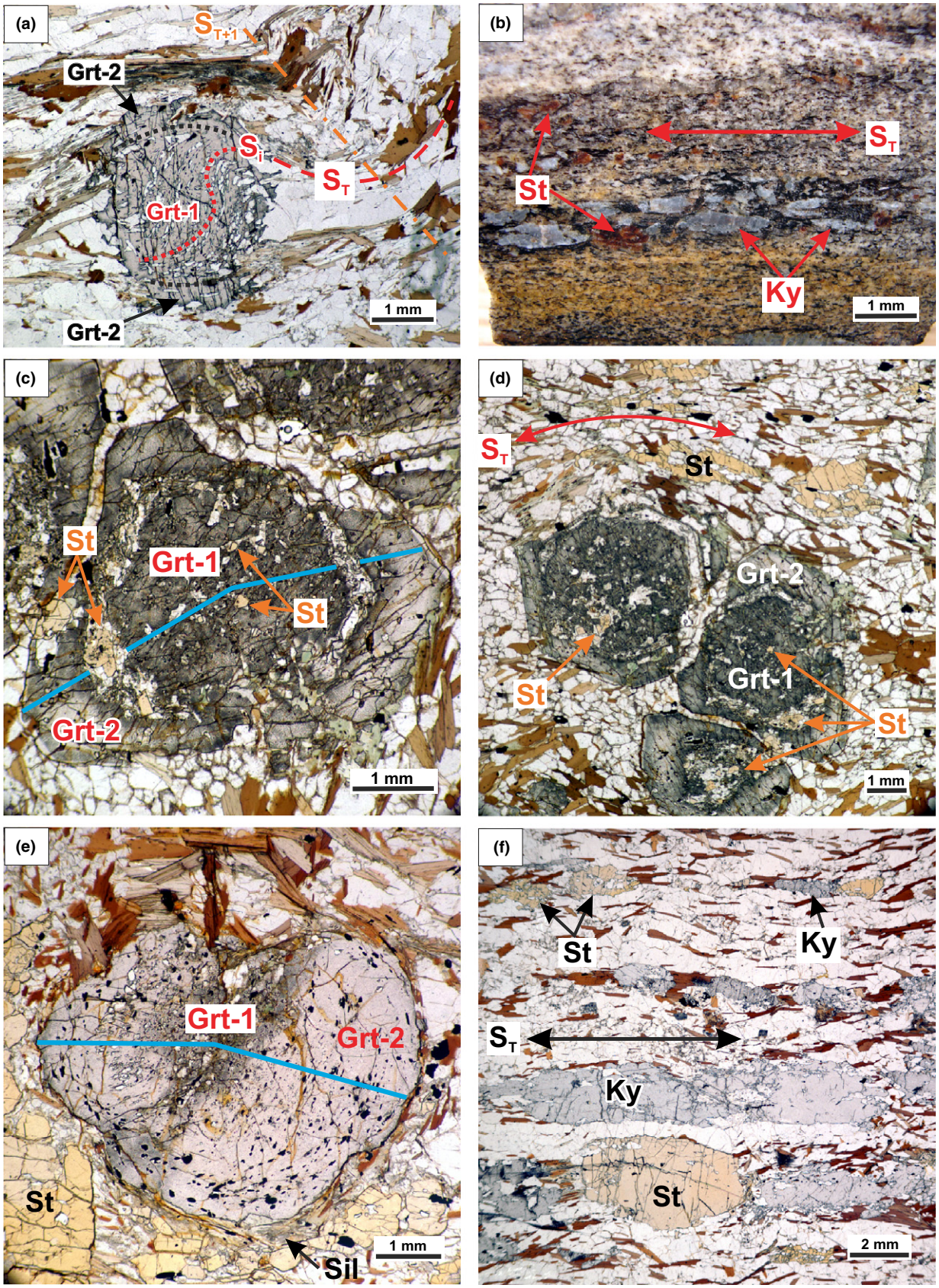

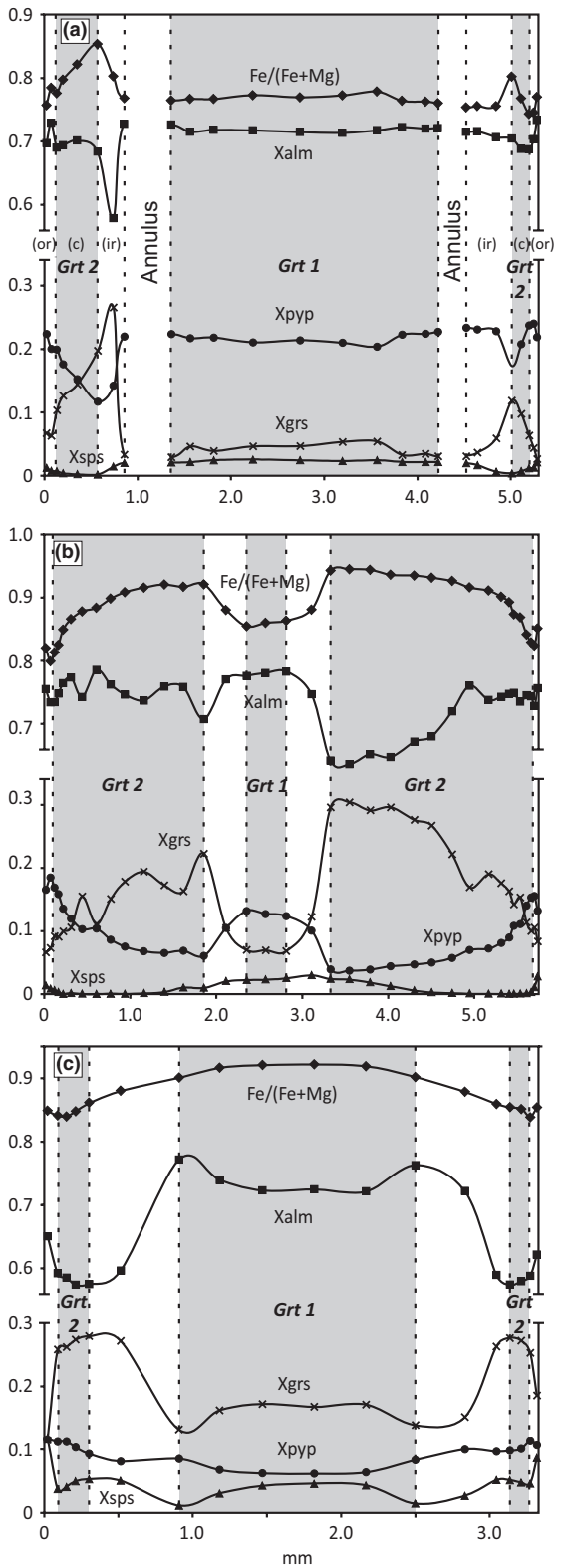

Figure 4. Compositional profiles across garnet porphyroblasts. (a) Sample 1. Abbreviations for Grt-2: ir, inner rim; c, core; or, outer rim. Note the sharp compositional gradient between vertical dashed lines. (b) Sample 2. (c) Sample 3. Grey shading shows the boundaries of garnet 1 and garnet 2.

retrograde diffusional re-equilibration during resorption of garnet (Kohn & Spear, 2000). Within sample 1, the replacement of Grt-1 and the outer portion of Grt-2, as well as the interface (annulus) between them, by the same assemblage (St-Plg-Mnz) suggests garnet was resorbed both from the inside and outside following growth of both Grt-1 and Grt-2. This is supported by the similarity in the composition of the complexly zoned garnet at its interface with the replacement products in the core, annulus, and outer atoll locations–a composition attributed above to garnet resorption during retrogression. The slightly higher Fe/(Fe + Mg) and grossular contents within the core of Grt-1 from sample 1 suggest incomplete diffusional re-equilibration across Grt-1 during retrogression.

More calcic plagioclase occurs adjacent to resorbed portions of garnet in all samples and at the rims of matrix grains, and thus, may likewise reflect the precipitation of new plagioclase upon garnet resorption during decompression (e.g., Spear *et al.*, 1990). The alternative that this more calcic plagioclase is due to the progressive consumption of a Ca-bearing phase such as epidote is considered less likely as this mineral is not preserved as inclusions in garnet. The less calcic cores of matrix plagioclase and those at a distance from garnet likely record equilibrium compositions along the prograde path or an earlier metamorphic event. Thus, the most reliable *P–T* conditions derive from the composition of minerals associated with the calcic plagioclase. Conventional barometric calculations will therefore yield a minimum estimate of near-peak *P–T* conditions.

P–T–D HISTORY

Stage-1 *P–T–d* history

The earliest phase of deformation and metamorphism is recorded in the syn-kinematic, inclusion-rich core (Grt-1) of a two-stage garnet. A sigmoidal inclusion trail within the garnet core indicates non-coaxial shear, synchronous with the development of the dominant penetrative foliation (S_T). Due to the lack of suitable inclusions within the Grt-1 core, the preserved growth zoning within samples 2 and 3 is the only indicator of the *P–T* evolution during the first stage of garnet growth. Garnet isopleth thermobarometry (e.g. Vance & Mahar, 1998) was used to estimate the *P–T* conditions of this earliest garnet growth event. Isopleths of spessartine, almandine and pyrope corresponding to the Grt-1 core composition in sample 2 intersect tightly at ~600 °C and 8 kbar (Fig. 6). Compositional isopleths corresponding to the centre of Grt-1 in sample 3 do not intersect at a point, but define a narrow field from 565 to 585 °C and from 7.8 to 8.5 kbar. The near vertical slope of X_{Pyp} isopleths implies Grt-1 of samples 2 and 3 grew along a *P–T* path of increasing temperature. The out-

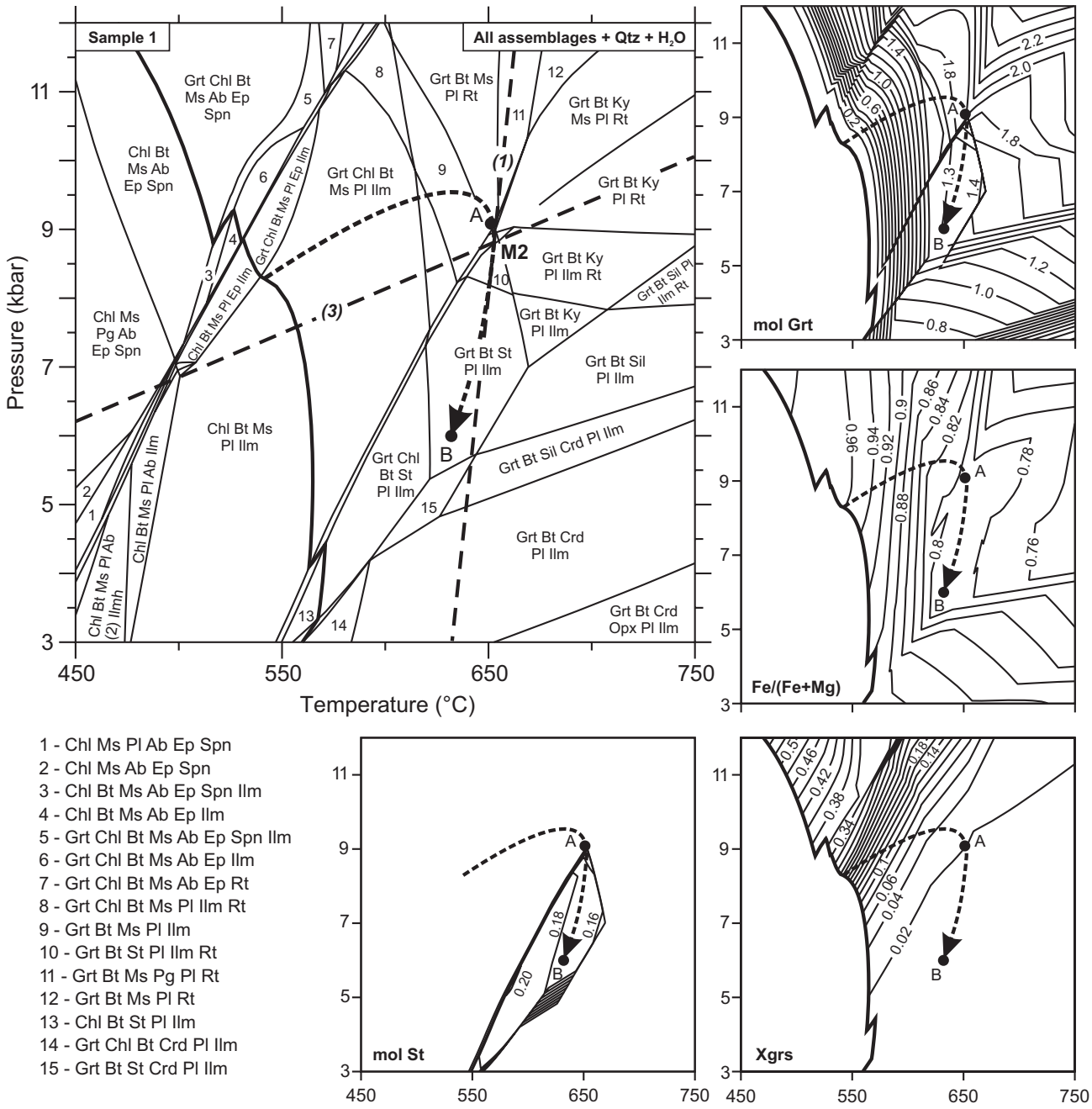

Figure 5. Isochemical phase diagram and molar isopleth sections calculated from the normalized effective bulk rock composition (Table 2b) of sample 1 in the chemical system MnNCKFMASHTO. H_2O and quartz calculated as in excess. Dashed lines display stage-2 garnet multi-equilibria thermobarometric estimates, with the stage-2 peak metamorphic estimate labelled M2, and each equilibria numbered as referenced in text. Our preferred stage-2 *P–T* path interpretation is shown by a dashed arrow (see text for discussion). The molar abundances of the main phases, shown in Fig. 7, are calculated along the path from points A to B.

ward decreasing grossular content within Grt-1 indicates these rocks followed a prograde *P–T* trajectory along shallower slope than X_{Grs} isopleths. Due to the absence of monazite inclusions within the garnet core, there is presently no upper age constraint on the timing of this metamorphic and deformational event. Grt-1 growth may be as old as Late Permian, similar to the metamorphic domain to the west, but we cannot rule out that it may be as young as Late Jurassic in age.

Stage-2 *P–T-d* history

Growth of euhedral to subhedral inclusion-poor garnet (Grt-2) during a discrete, later metamorphic event is supported by the following: (i) a large chemical

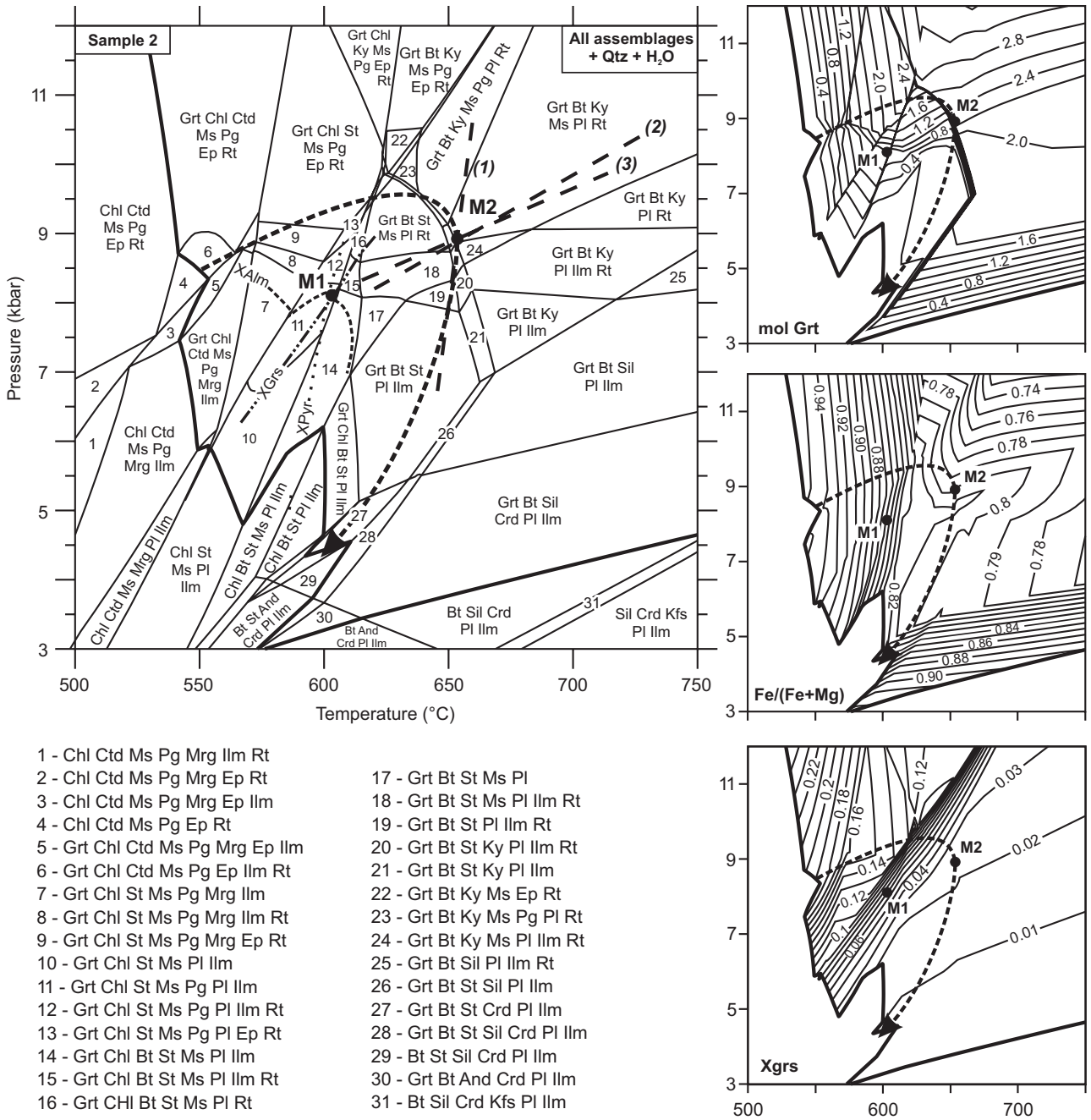

1 - Chl Ctd Ms Pg Mrg Ilm Rt
2 - Chl Ctd Ms Pg Mrg Ep Rt
3 - Chl Ctd Ms Pg Mrg Ep Ilm
4 - Chl Ctd Ms Pg Ep Rt
5 - Grt Chl Ctd Ms Pg Mrg Ep Ilm
6 - Grt Chl Ctd Ms Pg Ep Ilm Rt
7 - Grt Chl St Ms Pg Mrg Ilm
8 - Grt Chl St Ms Pg Mrg Ilm Rt
9 - Grt Chl St Ms Pg Mrg Ep Rt
10 - Grt Chl St Ms Pl Ilm
11 - Grt Chl St Ms Pg Pl Ilm
12 - Grt Chl St Ms Pg Pl Ilm Rt
13 - Grt Chl St Ms Pg Pl Ep Rt
14 - Grt Chl Bt St Ms Pl Ilm
15 - Grt Chl Bt St Ms Pl Ilm Rt
16 - Grt CHl Bt St Ms Pl Rt
17 - Grt Bt St Ms Pl
18 - Grt Bt St Ms Pl Ilm Rt
19 - Grt Bt St Pl Ilm Rt
20 - Grt Bt St Ky Pl Ilm Rt
21 - Grt Bt St Ky Pl Ilm
22 - Grt Bt Ky Ms Ep Rt
23 - Grt Bt Ky Ms Pg Pl Rt
24 - Grt Bt Ky Ms Pl Ilm Rt
25 - Grt Bt Sil Pl Ilm Rt
26 - Grt Bt St Sil Pl Ilm
27 - Grt Bt St Crd Pl Ilm
28 - Grt Bt St Sil Crd Pl Ilm
29 - Bt St Sil Crd Pl Ilm
30 - Grt Bt And Crd Pl Ilm
31 - Bt Sil Crd Kfs Pl Ilm

Figure 6. Isochemical phase diagram and molar isopleth sections calculated from the normalized effective bulk rock composition (Table 2b) of sample 2 in the chemical system MnNCKFMASHTO. H_2O calculated as in excess. *P–T* conditions of the incipient stages of stage-1 garnet growth (M1) are estimated from the intersection of X_{Alm} (dashed), X_{Pyr} (dotted), and X_{Grs} (dotted/dashed) isopleths corresponding to the Grt-1 core composition of sample 2. Dashed lines display stage-2 garnet multi-equilibria thermobarometric estimates, with the stage-2 peak metamorphic estimate labelled M2, and each equilibria numbered as referenced in text. The interpreted stage-2 *P–T* path is shown by a dashed arrow.

gradient/discontinuity at the boundary between the inclusion-rich core (Grt-1) and inclusion-poor overgrowth (Grt-2); and (ii) an increase in Fe/(Fe + Mg) and X_{Grs}, and a decrease in X_{Alm} and X_{Pyp} values from Grt-1 to Grt-2, which does not conform to a prograde path involving garnet growth (Fig. 6).

Multi-equilibria thermobarometric estimates are presented in Figs 5 & 6 and Table 3. In order to minimize the effects of retrograde diffusion, near thermal peak thermobarometric estimates of stage-2 garnet growth were calculated from minimum Fe/(Fe + Mg) values just inboard of the Mn- and

Fe-enriched outer rim, together with the rims of plagioclase and the least Fe-enriched biotite. Thermobarometric estimates of stage-2 garnet growth for samples 1–3 range between 650–680 °C and 8–10 kbar. Garnet and plagioclase in samples 1 and 2 have low grossular and anorthite contents, which reduces the reliability of the geobarometric estimates (Ashworth & Evirgen, 1985; Todd, 1998). Part of the inaccuracy associated with low-anorthite contents may have been addressed here by using the plagioclase model of Aranovich (1991), which Aranovich found yields lower pressures for sodic plagioclase that are more consistent with independent estimates. Despite a potential inaccuracy associated with low grossular contents for Grt-2 of samples 1 and 2, the barometric estimates are consistent with the more reliable results of the more calcic mineral compositions in sample 3. Florence & Spear (1993) noted that diffusional modification of a sharp compositional gradient within garnet due to an intermittent period of garnet dissolution during staurolite growth along the prograde path will shift Fe/(Fe + Mg) at the garnet rim to a higher value, yielding a calculated temperature lower than the true thermal peak. Therefore, the slightly higher peak *P–T* estimates of 680 °C and 9–10 kbar from sample 3, in which staurolite is absent, may be a closer estimate to near-peak stage-2 *P–T* conditions.

Conventional multi-equilibria thermobarometric estimates of peak stage-2 garnet growth are consistent with the presence of kyanite in sample 2. However, the *P–T* estimates of sample 2 lie on the upper thermal stability limit of staurolite (Fig. 6), yet well within overall uncertainties of thermobarometric and phase diagram calculations. Nevertheless, garnet-biotite thermometric estimates may overestimate peak temperatures if biotite was enriched in Fe during garnet resorption. Arguing against this caveat is the abrupt decrease of Fe/(Fe + Mg) in biotite >300 μm from garnet (see above), with little Fe/(Fe + Mg) variation beyond this distance, suggesting that Fe-enrichment of biotite during garnet resorption was fairly restricted. Therefore, temperatures calculated from biotite with the lowest Fe/(Fe + Mg) composition are expected to yield a close approximation to peak temperatures. Alternatively, a small apparent discrepancy between thermobarometric estimates and equilibrium assemblage modelling may reflect the metastable persistence of staurolite above its upper thermal stability limit (e.g., Waters & Lovegrove, 2002; Pattison & Tinkham, 2009; Pattison *et al.*, 2011). The syn- to post-kinematic staurolite and kyanite in samples 2 and 4 is interpreted to have grown and equilibrated with Grt-2. This is based on the agreement between Grt-2 thermobarometry and the predicted stability fields of staurolite and kyanite, as well as the syn- to post-kinematic nature of staurolite, kyanite and Grt-2.

By contrast, the origin of prograde, matrix staurolite in sample 1 differs from the stage-2 paragenesis and its possible metastable existence in sample 2. Contrary to the near ubiquitous static recrystallization textures associated with stage-2 metamorphism, matrix staurolite of sample 1 has an anhedral and skeletal nature, and is aligned parallel to the foliation and is deflected around garnet (Fig. 3d), indicative of syn-kinematic growth. Though it remains unknown as to which garnet generation this staurolite is deflected around, the syn-kinematic stage-1 garnet core within other samples seems to be a more likely candidate. Based on these textures, it is interpreted that matrix staurolite within sample 1 is from an earlier metamorphic event, likely related to stage-1 garnet.

Stage-2 retrograde *P–T* history

The *P–T* path is constrained for sample 1 by the production of staurolite from garnet and from the Ca-rich composition (X_{Grs} = 0.25) of the Grt-2 core. Although it is possible to produce staurolite with isobaric heating up to the peak temperature (M2, Fig. 5), this path is interpreted as unlikely since garnet resorption is negligible even near the metamorphic peak (Fig. 5). Preference is given to a clockwise, looping *P–T* path in which staurolite growth and garnet resorption accompany the onset of decompression after peak *P–T* conditions. The retrograde segment of the path is constrained to be consistent with the absence of retrograde sillimanite in samples 1 (appearing above 620 °C and 5.4 kbar) and 2, yet consistent with the presence of cordierite rims around staurolite in samples 2 and 4, and retrograde sillimanite in sample 4. These observations require decompression below 5 kbar prior to cooling below 600 °C (Fig. 6).

To highlight the consistency between observed mineral modes and reaction textures with that predicted for this steep to near isothermal decompression path within the model system, molar mineral abundances were calculated for sample 1 (Fig. 7) and plotted based on the retrograde *P–T* path between points A and B in Fig. 5. At 9 kbar and at near- peak conditions of metamorphism (point A in Fig. 5), muscovite and garnet are stable along with biotite and plagioclase. Early in the retrograde history, at 8.8 kbar, staurolite growth is predicted, together with plagioclase and biotite, at the expense of muscovite and garnet (Fig. 7). Upon decompressing through 8.6 kbar, muscovite is entirely consumed, consistent with its absence in the observed mineral assemblage, and below which staurolite remains stable. This modelling is consistent with the observed assemblage of staurolite, plagioclase and Y-rich monazite within resorbed portions of both stage-1 and 2 garnet of sample 1, and retrograde biotite recorded texturally as randomly oriented matrix grains and within the cores of atoll garnet. The presence of monazite within the resorbed garnet, and its otherwise complete absence as an included phase within both stage-1 and 2 garnet suggests that this monazite was an accessory product of these garnet and muscovite-consuming reactions.

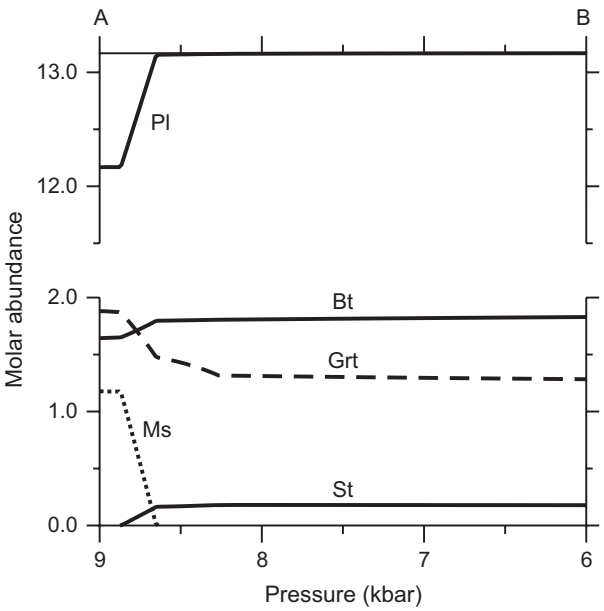

Figure 7. Diagram showing the evolution of the molar abundance in sample 1 of the main phases as calculated along the *P–T* path from point A to B in Fig. 5.

As discussed below, the consistently younger ages and distinctly high Y-content of monazite intimately associated with euhedral, inclusion-free staurolite within resorbed portions of both stage-1 and -2 garnet of sample 1, corroborates the interpretation that these staurolite grains grew at the expense of garnet following growth of the stage-2 garnet rims.

MONAZITE GEOCHRONOLOGY

Geochronological methods

Prior to U-Th-Pb analysis, the locations of all monazite grains in thin section were identified using an automated scanning routine on a Zeiss EVO 50 series scanning electron microscope (SEM) at the Geological Survey of Canada in Ottawa, operating at 20 kV accelerating voltage and 500 pA beam current. Back scattered electron (BSE) images of the *in situ* monazite grains were also obtained to provide insight into their petrological context and internal zoning, identify cracks and mineral inclusions, and to guide analytical spot placement. In order to better characterize chemical zonation and potential age domains within individual monazite grains, chemical X-ray maps of Y, U, Th and Ca in strategically selected monazite grains were produced using a Cameca SX50 electron microprobe at the University of Massachusetts operating at a high current (240–260 nA), with small step sizes (0.25–0.62 μm), and rastering of the electron beam. For each of the Y maps, the approximate Y concentration in ppm for each pixel was calculated using the AgeMap program (Williams *et al.*, 1999; modified by Goncalves *et al.*, 2005) in order to estimate the approximate Y concentration for each SHRIMP spot (Table 4).

Table 4. SHRIMP U-Th-Pb analytical data for monazite.

Spot[a]	Texture[b]	Grain location	Y (ppm)[c]	Th/U	$^{204}Pb/^{206}Pb$	f(206)^{207} (%)[d]	Total $^{207}Pb/^{206}Pb$	Total $^{238}U/^{206}Pb$	Age (Ma)[e,f] $^{206}Pb/^{238}U$
Sample 1									
M131.1	Matrix || S_T	core	400	8.64	1.039E-03 ± 1.143E-04	1.67	0.0594 ± 0.0006	52.316 ± 0.628	120.4 ± 1.4
M102.1	Replaced Grt	core	1400	7.43	1.144E-03 ± 1.716E-04	1.64	0.0591 ± 0.0010	54.822 ± 0.877	115.0 ± 1.8
M102.2	Replaced Grt	rim	3400	6.39	2.215E-03 ± 1.329E-04	4.01	0.0780 ± 0.0026	56.004 ± 0.672	109.9 ± 1.4
M9.1	Replaced Grt	core	1700	2.82	4.817E-04 ± 6.263E-05	1.15	0.0552 ± 0.0005	56.010 ± 0.672	113.1 ± 1.4
Sample 2									
M55.1	St	core	5800	5.35	6.104E-04 ± 6.714E-05	0.98	0.0539 ± 0.0004	53.241 ± 0.639	119.1 ± 1.5
M55.2	St	rim	5200	6.44	8.427E-04 ± 9.269E-05	1.52	0.0582 ± 0.0006	54.034 ± 0.540	116.8 ± 1.2
M156.1	St	rim	8500	7.50	9.815E-04 ± 1.080E-04	1.68	0.0595 ± 0.0011	54.207 ± 0.759	116.2 ± 1.6
M157.1	St	N/A	8500	9.19	1.112E-03 ± 1.223E-04	1.45	0.0576 ± 0.0009	53.001 ± 0.742	119.1 ± 1.7
M157.2	St	N/A	6500	4.18	4.238E-04 ± 5.085E-05	9.33	0.0535 ± 0.0004	53.004 ± 0.583	119.7 ± 1.3
M118.1	Matrix ‖ S_T	core	2300	4.53	4.112E-04 ± 6.169E-05	0.77	0.0522 ± 0.0006	53.624 ± 0.590	118.5 ± 1.3
M118.2	Matrix ‖ S_T	rim	5500	6.71	7.765E-04 ± 9.317E-05	1.43	0.0574 ± 0.0006	55.046 ± 0.661	114.7 ± 1.4
Sample 4									
M144.1	Ky || S_T	rim	11000	6.45	9.508E-04 ± 9.508E-05	1.50	0.0580 ± 0.0005	53.439 ± 0.748	118.1 ± 1.6
M123.1	Matrix || S_T	core	14000	2.83	3.323E-04 ± 3.988E-05	0.79	0.0523 ± 0.0004	52.814 ± 0.634	120.4 ± 1.4
M107.1	Crd || S_T	rim	10 000	7.71	8.232E-04 ± 9.055E-05	1.10	0.0548 ± 0.0010	54.144 ± 0.653	117.0 ± 1.4
M246.1	Crd || S_T	core	15 000	4.63	2.726E-04 ± 6.271E-05	0.76	0.0521 ± 0.0004	55.165 ± 0.591	115.3 ± 1.2
M246.2	Crd || S_T	rim	10 000	5.84	5.949E-04 ± 9.518E-05	1.42	0.0574 ± 0.0005	55.265 ± 0.653	114.3 ± 1.3
M511.1	Matrix	core	13 500	5.73	4.610E-04 ± 7.376E-05	1.06	0.0545 ± 0.0004	53.780 ± 0.743	117.9 ± 1.6
M511.2	Matrix	rim	3700	8.69	8.827E-04 ± 8.827E-05	1.27	0.0562 ± 0.0005	54.366 ± 0.577	116.3 ± 1.2
M511.3	Matrix	core	13 500	5.21	4.710E-04 ± 5.181E-05	0.83	0.0527 ± 0.0004	53.599 ± 0.595	118.5 ± 1.3
M516.1	Matrix	rim	6800	7.50	6.238E-04 ± 9.357E-05	1.05	0.0544 ± 0.0011	54.233 ± 0.875	116.9 ± 1.9
M516.2	Matrix	core	17 300	5.17	3.895E-04 ± 5.842E-05	0.77	0.0522 ± 0.0007	53.687 ± 0.842	118.4 ± 1.8
M516.3	Matrix	rim	6800	9.71	8.472E-04 ± 7.625E-05	1.30	0.0564 ± 0.0005	54.064 ± 0.617	117.0 ± 1.3

[a]Spot: M157.2 = 2nd spot on monazite grain #157.
[b]Texture: location of monazite as inclusion in St, Ky, Crd, or as a matrix grain (|| = elongate monazite grain parallel to foliation).
[c]Y: approximate Y concentration calculated from Y X-ray maps using the AgeMap program as modified by Goncalves *et al.* (2005).
[d]f(206)207 refers to the fraction of total ^{206}Pb that is common Pb, calculated using the 207Pb-method.
[e]Ages have been corrected for common Pb using the ^{207}Pb-method.
[f]Uncertainties reported at 1σ (absolute) and are calculated by numerical propagation of all known sources of error (Stern & Berman, 2000).

In situ U-Th-Pb analyses using the SHRIMP II at the Geological Survey of Canada in Ottawa were performed on monazite cored from polished thin sections and mounted in epoxy together with pre-polished monazite standards according to the methods of Rayner & Stern (2002). Targeted areas of monazite were analyzed using a mass-filtered O_2^- primary beam focused with a Kohler aperture to a spot measuring 9×12 μm. The methods employed follow the SHRIMP analytical protocols described in detail by Stern (1997), Stern & Sanborn (1998) and Stern & Berman (2000). Tera-Wasserburg and Concordia plots, data regression and weighted mean calculations were made using the program ISOPLOT 3.7 (Ludwig, 2008). Errors assigned to SHRIMP U–Th–Pb ages were determined using numerical propagation of all known sources of error as outlined by Stern (1997), Stern & Sanborn (1998), and Stern & Berman (2000). Uncertainties for individual analyses (ratios and ages) shown in Tables 4 and S1, and error ellipses shown in Fig. 8, are presented at the 1σ level, whereas weighted mean ages and 2σ uncertainties are provided in the text, Table 3 and Fig. 8.

Geochronological results

A plot of the monazite SHRIMP data for sample 4 on a conventional (Wetherill) U-Pb concordia diagram reveals a reverse discordance exhibited by some monazite analyses (Fig. 8d). Excess ^{206}Pb due to incorporation of ^{230}Th into monazite at the time of crystallization will lead to an overestimation of ^{206}Pb/^{238}U ages and reverse discordance paralleling the ^{206}Pb/^{238}U axis on conventional U-Pb concordia diagrams (Schärer, 1984). Our data show a subtle trend of increasing reverse discordance with increasing ^{208}Pb/^{206}Pb (the radiogenic proxy of Th/U), which indicates that to some minor degree the reverse discordance may be the result of excess ^{206}Pb due to ^{230}Th disequilibrium. Unfortunately the ^{208}Pb/^{232}Th chronometer, which is ideal for monazite since it is not known to be affected by isotopic disequilibrium (i.e., unsupported ^{206}Pb), cannot be used in this study because one of the three monazite standards routinely yielded a high Th-Pb age possibly due to an indeterminate matrix effect. This creates an unquantifiable uncertainty in the Th-Pb ages for the monazite.

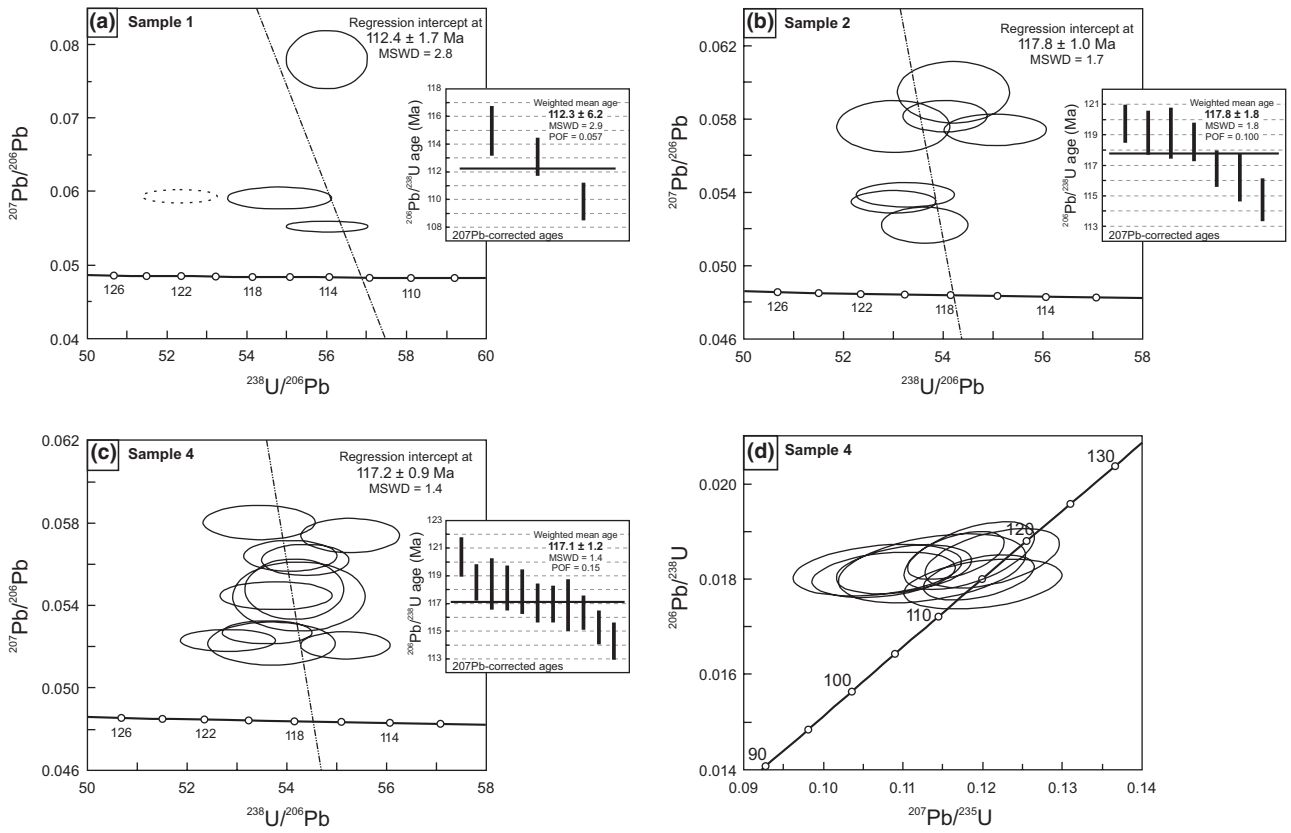

Figure 8. U-Pb isotopic plots for samples 1, 2 and 4. (a–c) Tera–Wasserburg plots for samples 1, 2 and 4 showing isotopic data uncorrected for common Pb. Regression is fitted through a Late Cretaceous common Pb isotopic composition (Stacey & Kramers, 1975). Dashed ellipse excluded from the regression (see text for discussion). Error ellipses represent 1σ level of uncertainty. Inset shows distribution of (^{207}Pb-corrected) ^{206}Pb/^{238}U ages, with error bars at 1σ. Bold horizontal line is reference mean age. (d) Concordia plot for monazite from sample 4. Note the horizontal trend parallel to the ^{207}Pb/^{235}U axis in the discordant data.

However, this problem seems to have affected only one-third of the standards, so it is likely some, or possibly all, of the monazite unknowns were similarly unaffected. Consequently, given that the $^{206}Pb/^{238}U$ ages are consistently younger than $^{208}Pb/^{232}Th$ ages (Table S1) would suggest these grains do not contain significant excess ^{206}Pb. Additionally, when applying the excess ^{206}Pb correction of Schärer (1984) it at most produces an excess in age of 1.2–1.9 Ma, which is no greater than analytical error, even for monazite that grew from a metamorphic fluid with extremely low Th/U (0.3–0.7) and had a large amount of Th fractionation. Thus, despite any minor excess of ^{206}Pb, we are confident the $^{206}Pb/^{238}U$ ages will provide reasonably accurate constraints within the resolution required for this study to differentiate the metamorphic and deformation events.

We can infer a further reduction in the significance of the contribution of excess ^{206}Pb to reverse discordance based on analyses from sample 4. These analyses do not plot in a vertical trend above concordia, as would be expected if the reverse discordance was due to excess ^{206}Pb. Rather, the analyses trend to the left of concordia parallel to the $^{207}Pb/^{235}U$ axis (Fig. 8d). This trend is interpreted to be largely the result of an overcorrected $^{207}Pb/^{235}U$ ratio using the ^{204}Pb method. The errors arising from low ^{204}Pb counts, background interference and a 204 isobar, can overcorrect for common Pb, which most adversely affects young samples with relatively low concentrations of ^{207}Pb.

For the sake of thoroughness, the analyses were corrected for common Pb based on the ^{204}Pb (Table S1) and ^{207}Pb (Table 4) methods following the procedure of Stern & Berman (2000) and Ireland & Gibson (1998). The two correction methods yield ages indistinguishable within error. However, all things considered, the $^{206}Pb/^{238}U$ chronometer corrected using the ^{207}Pb method is thought to provide the most meaningful ages for this study; accordingly, all ages quoted and displayed on Tera-Wasserburg concordia diagrams (Fig. 8a–c) are based on the $^{206}Pb/^{238}U$ chronometer.

Sample 1

Analyses of monazite within sample 1 were obtained on a single matrix grain, as well as two monazite crystals that occur together with plagioclase and euhedral staurolite within replacement textures inside garnet (Fig. 9a,b). Elongated matrix monazite is consistently aligned parallel to S_T. The matrix grain, monazite 131 (Fig. 9c), is acicular, measuring <35 μm in shortest dimension and up to 165 μm in the longest dimension, and is approximately parallel to the foliation (S_T). Monazite 131 has a broad, uniform low Y (<700 ppm) core surrounded by a thin (<5 μm) Y-depleted zone, and a thin (<5 μm) Y-rich rim. A single spot analysis of the low-Y core of this matrix monazite yields an age of 120.4 ± 1.4 Ma. Grain 102 (Fig. 9a) is a subhedral, 20 × 45 μm grain that occurs with plagioclase and euhedral staurolite within a resorption ring between Grt-1 and -2. Grain 102 has a uniform, moderate-Y (700–1500 ppm) core and high-Y (2000–3400 ppm) rim, with a sharp boundary between the two zones. Spot analyses of the moderate-Y core and high-Y rim yield ages of 115.0 ± 1.8 Ma and 109.9 ± 1.4 Ma, respectively. Grain 9 (Fig. 9b) is a subhedral, 30 × 50 μm grain that occurs together with plagioclase and euhedral staurolite within a resorbed hole inside Grt-1. Monazite nine has a fairly uniform moderate-Y concentration (1000–2000 ppm), and a very thin (<5 μm) high-Y (3500–4000 ppm) rim. A single analysis from the centre of grain nine yields a $^{206}Pb/^{238}U$ age of 113.1 ± 1.4 Ma.

Sample 2

Analyses of monazite within sample 2 were obtained on three inclusions within two different staurolite porphyroblasts (Fig. 9d,e), and a single matrix grain. Two of the monazite inclusions within staurolite are anhedral to subhedral grains that are ~30 × 100 μm. The third inclusion within staurolite is very elongated, ~160 μm in the longest dimension oriented roughly parallel to a weakly defined and statically overprinted external foliation (S_T). Only one of the three inclusions within staurolite is intersected by a very fine micro-crack (Fig. 9e). X-ray mapping revealed three distinct compositional domains within monazite included in staurolite and in the matrix: (i) moderate-Y, high-Th core; (ii) an intermediate low-Y, low-Th zone; and (iii) high-Y, moderate-Th rim. Despite the different textural positions and discrete chemical domains, both the core and outer high-Y rim yield a restricted range of ages between 119.7 ± 1.3 Ma and 114.7 ± 1.4 Ma (see Table 4) that are interpreted to form a single population with a weighted mean age of 117.8 ± 1.7 (MSWD = 1.8) (Fig. 8b).

Sample 4

Analyses of monazite from sample 4 were obtained on one inclusion in kyanite, two inclusions in cordierite and two matrix grains. Monazite inclusions within cordierite and syn-kinematic kyanite are elongate, euhedral to subhedral grains, >30 μm in the shortest dimension and up to 200 μm in the longest dimension. Elongate monazite inclusions within kyanite and cordierite, as well as matrix grains, are aligned parallel to S_T, which is defined by the rutile trains and aligned kyanite and staurolite (Fig. 9f). All monazite grains, regardless of textural location, show similar concentrations and compositional zoning patterns characterized by a Y-rich (12 000–18 000 ppm) core surrounded by a uniform zone relatively depleted in

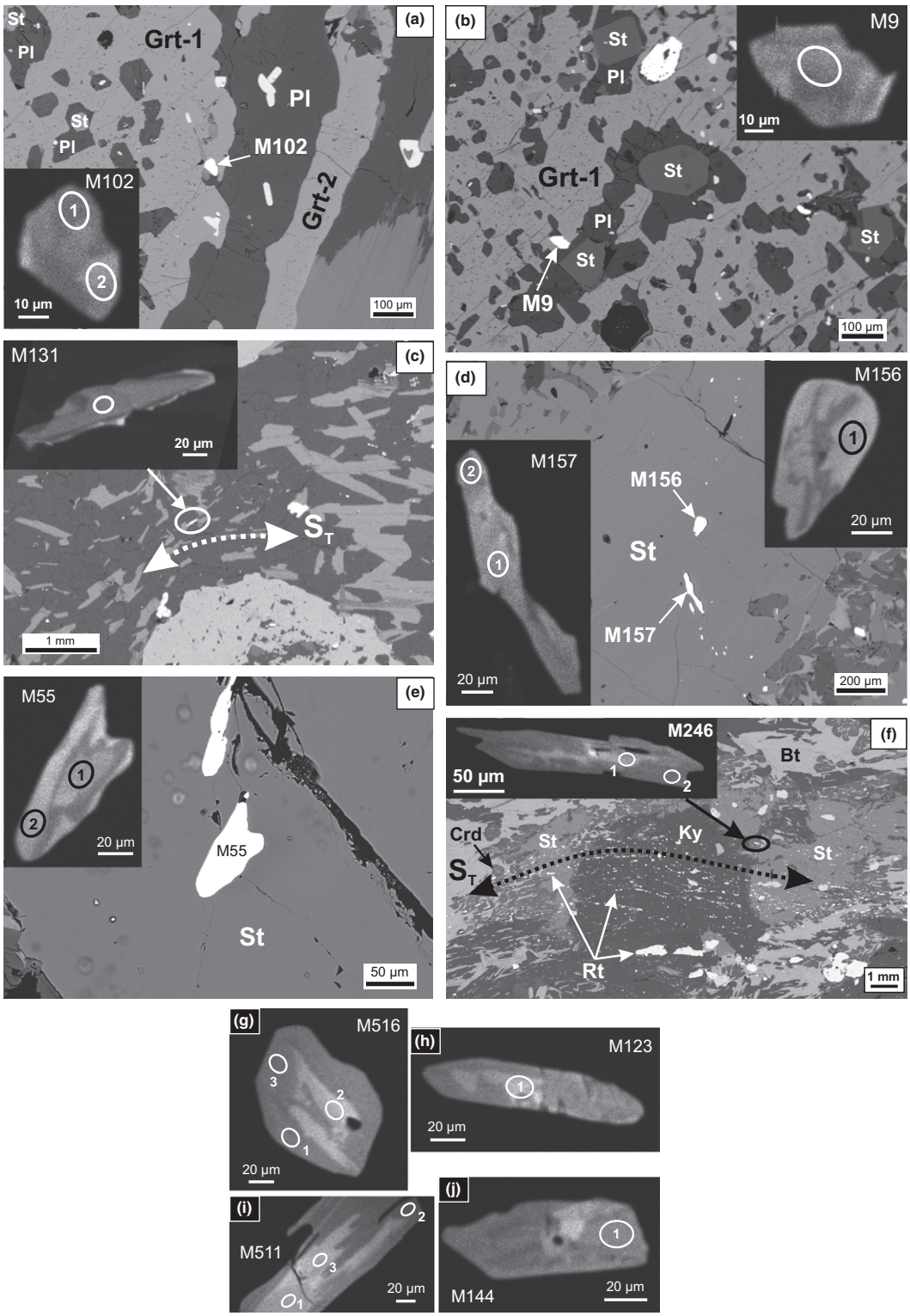

Figure 9. SEM backscattered images of monazite and the surrounding area in samples 1, 2 and 4. Ellipses on inset Yttrium (Y) X-ray maps of monazite show the location of SHRIMP analysis spots. Lighter shades of grey on Y maps indicate relatively higher concentration. (a) M102 and (b) M9, both associated with staurolite and plagioclase within heavily resorbed garnet porphyroblasts in sample 1. (c) Elongate matrix monazite M131 aligned near parallel to the transposition foliation (S_T). (d) M156 and M157, and (e) M55, within staurolite from sample 2. (f) Elongate monazite, M246, aligned parallel to the relict transposition foliation (S_T) in sample 4, which is defined by rutile trains within the matrix, and as inclusion trains within porphyroblasts of kyanite, staurolite and cordierite. (g–j) Y maps of monazite grains from sample 4.

Y (6000–10 000 ppm) (Fig. 9g–j). This Y zoning is mimicked by Th. In spite of the observed textural and chemical differences described here, all 11 analyses of these five monazite grains form a single population with a weighted mean $^{206}Pb/^{238}U$ age of 117.1 ± 1.2 Ma (MSWD = 1.4) (Fig. 8c).

In contrast to samples 1 and 2, there is no high-Y rim observed in monazite from sample 4. This is interpreted to be due to the relatively small amount of garnet observed in sample 4. In this garnet-poor sample there would not be a significant amount of Y tied up in garnet, nor excess Y released upon garnet breakdown.

Interpretation of geochronological data – constraining a Cretaceous *P–T* path

It is unlikely that the monazite ages have been reset by diffusive Pb loss. Based on experimentally determined diffusion parameters, Cherniak *et al.* (2004) and Gardés *et al.* (2006) have determined that monazite would have to be exposed to temperatures >800 °C for a geologically unrealistic length of time for there to be any appreciable Pb loss, and predict closure temperatures comparable to zircon (i.e. 900 °C). These conclusions are consistent with numerous observations of sharp boundaries between domains of contrasting Pb concentrations, and the preservation of significantly older ages through younger granulite facies metamorphic events (e.g. DeWolf *et al.*, 1993; Spear & Parrish, 1996; Braun *et al.*, 1998; Cocherie *et al.*, 1998; Crowley & Ghent, 1999; Zhu & O'Nions, 1999). Given the peak temperature estimates for these samples (~650–680 °C), we interpret that these grains have not been reset due to Pb loss by thermally-activated volume diffusion.

More plausibly, several studies (Seydoux-Guillaume *et al.*, 2002; Harlov & Hetherington, 2010; Hetherington *et al.*, 2010; Harlov *et al.*, 2011; Williams *et al.*, 2011) have shown that monazite ages may be reset by fluid-assisted coupled dissolution-reprecipitation, which may operate at temperatures well below the closure temperature of monazite. Unlike the matrix grains, monazite inclusions in staurolite are shielded from an intergranular fluid, and should therefore retain their primary metamorphic age. However, if monazite inclusions in staurolite are intersected by a microcrack within the third dimension, this could provide a pathway for fluid assisted dissolution, reprecipitation and Pb loss. Williams *et al.* (2011) examined the resetting of monazite ages during fluid-related coupled dissolution-reprecipitation, and observed that altered rims yield a scattering of reset ages, whereas the age of unaltered monazite cores were largely unaffected. Contrary to the results of Williams *et al.* (2011), the ages obtained from distinct core-rim compositional domains of monazite inclusions in staurolite from this study (Fig. 9e) agree within error (Table 4), leaving no indication that these grains have been affected by fluid-assisted coupled dissolution-reprecipitation. Ages from these grains are therefore interpreted as primary metamorphic ages. Furthermore, because monazite both in the matrix and included in staurolite yield a single age population, we interpret matrix monazite to also preserve their primary metamorphic age.

Timing of stage-2 metamorphism and deformation

Nineteen $^{206}Pb/^{238}U$ analyses from all 11 monazite grains (excluding the Y-rich monazite within resorbed Grt-2 of sample 1) yield a single age population at 117.5 ± 0.9 Ma (MSWD = 1.7). The incorporation of *c.* 118 Ma monazite within syn- to post-kinematic, stage-2 porphyroblasts of staurolite and kyanite indicates this population of monazite grew prior to, or synchronous with, these near-peak stage-2 porphyroblasts. As discussed below, slightly younger ages (*c.* 112 Ma) from distinct, Y-rich monazite within resorbed portions of both stage-1 and 2 garnet of sample 1, are interpreted to have formed as garnet broke down during the onset of decompression following the peak of stage-2 metamorphism. The absence of monazite included in stage-1 garnet, and the limited time between prograde metamorphism (*c.* 118 Ma) and stage-2 decompression (*c.* 112 Ma) suggest it is unlikely the *c.* 118 Ma monazite population grew during stage-1 metamorphism. Instead the *c.* 118 Ma monazite population is interpreted to date stage-2 prograde metamorphism. Furthermore, the common alignment of monazite parallel to S_T in the matrix (Fig. 9c,f), and its inclusion in syn- to post-S_T porphyroblasts of staurolite and kyanite, suggests monazite grew during the waning phase of protracted development of S_T during prograde stage-2 metamorphism. The partially syn-kinematic nature of both Grt-1 and stage-2 staurolite and kyanite porphyroblasts with respect to S_T, suggests S_T is a composite D_1/D_2 transposition foliation in the sense of Williams (1983) and Tobisch & Paterson (1988). The presence of intrafolial isoclinal folds suggests this composite transposition foliation developed by isoclinal folding and rigid body rotation of the older D_1 foliation into parallelism with the new D_2 foliation, such that the elements defining the new foliation (S_T) are inherited from the old foliation (cf. Williams, 1983).

Approximately 1.2 km to the east of sample 2, slightly older Early Cretaceous dates were obtained by Berman *et al.* (2007a), who calculated an average $^{206}Pb/^{238}U$ age of 146 ± 3 Ma from three different monazite grains (sample 4 of Berman *et al.*, 2007a). Berman *et al.* interpreted these grains as primary inclusions within post-kinematic staurolite porphyroblasts that grew during a high-*P* (~9 kbar) metamorphic event. The *c.* 117.5 ± 0.9 Ma age determined in this study records the time at which these samples passed through the monazite growth reaction, which is a function of pressure, temperature and the bulk

composition. Given the considerable chemical variability between sample 4 of Berman *et al.* (2007a) (Ca/Na = 0.14) and that of samples 2 (Ca/Na = 0.56) and 4 (Ca/Na = 0.99) of this study, there is no reason to expect that the monazite-producing reactions were the same between the two studies. Nor should we expect that the reactions were operating under the same *P–T* conditions, and hence time. For example, Fitzsimons *et al.* (2005) demonstrated that variations in the evolving metamorphic mineral assemblages, between samples of contrasting composition in AFM space, resulted in the growth and preservation of monazite from different metamorphic reactions and under considerably different *P–T* conditions (e.g. greenschist- v. amphibolite facies). Janots *et al.* (2008) also found that monazite stability is sensitive to bulk composition. In their study of the stability and phase relations between allanite and monazite, Janots *et al.* (2008) offered the following generalized prograde reaction: Allanite + apatite + Al-Fe-Mg phases1 = monazite + anorthite + Al-Fe-Mg phases 2.

Janots *et al.* (2008) suggested that metapelites with a high Ca/Na ratio, and subsequently high anorthite activity in plagioclase, would shift the above equilibrium to the right, stabilizing allanite to higher temperature. Given the considerably higher Ca/Na and X_{An} contents from samples of the present study v. that of sample 4 of Berman *et al.* (2007a), it follows from Janots *et al.* (2008) that the monazite-after-allanite equilibrium would occur at higher temperatures in rocks of this study. Consequently, monazite in our study should yield younger ages for rocks following a clockwise *P–T* path, precisely as observed. We therefore interpret that prograde metamorphism may have occurred between 146 and 118 Ma in this region. Such protracted metamorphism, ~28 Ma does not seem unreasonable considering recent work which document a 25 Ma duration of eclogite facies conditions (Mattison *et al.*, 2006), and prograde garnet growth sustained over a 25–40 Ma interval (Skora *et al.*, 2009; Cheng *et al.*, 2011).

Timing of stage-2 retrogression and exhumation

Monazite grains M9 and M102 in sample 1 occur within resorbed portions of garnet associated with post-kinematic staurolite, and yield a weighted mean age of 112.3 ± 6.2 Ma (MSWD = 2.9) (Fig. 8a). This age is nominally younger than the 120.4 ± 1.4 Ma matrix monazite, but the difference is considered significant given their distinctly higher yttrium content (~1000–10 000 ppm Y) compared to the older matrix monazite (<500 ppm). Bea & Montero (1999) and Pyle & Spear (1999) determined that garnet and xenotime are the only significant reservoirs of yttrium in metapelitic rocks, and that the growth of garnet is accompanied by the consumption of xenotime. Given the large volume of garnet in these rocks, it follows that the majority of yttrium resides within garnet. Therefore, we interpret that the high-Y, younger monazite formed during the release of yttrium accompanying breakdown of garnet (e.g. Pyle & Spear, 1999; Foster *et al.*, 2002), which is interpreted to have occurred during decompression from the stage-2 metamorphic peak (~650–680 °C and 9 kbar) into the staurolite stability field. This conclusion is supported by the occurrence of 114.3 ± 1.3 Ma monazite within cordierite, which is constrained by phase relationships to have crystallized below ~5 kbar (Fig. 6) after *c.* 114 Ma. It is also consistent with results from 7–12 km northwest of sample 1, where 115–107 Ma relatively Y-rich monazite in two rocks formed during garnet resorption and re-equilibration at pressures less than 6 kbar (Berman *et al.*, 2007a). Finally, we note that these younger ages directly linked to decompression from peak stage-2 metamorphism further support our interpretation that the older ages (*c.* 118 Ma) for monazite inclusions within staurolite and kyanite date the prograde history of the ~9 kbar stage-2 metamorphic event.

TECTONIC IMPLICATIONS

Previous work in the Yukon-Tanana terrane of easternmost Alaska and west-central Yukon suggests the terrane was strongly transposed and metamorphosed to amphibolite facies in the Permo-Triassic (Dusel-Bacon *et al.*, 1995, 2002; Berman *et al.*, 2007a; Beranek & Mortensen, 2011), followed by a metamorphic overprint in the Early Jurassic before being exhumed to upper crustal levels in the Early to Middle Jurassic (Dusel-Bacon *et al.*, 1995, 2002; Hansen & Dusel-Bacon, 1998; Berman *et al.*, 2007a). However, the results of this study, together with the work of Berman *et al.* (2007a), indicate a more protracted and heterogeneous tectono-thermal history for the Yukon-Tanana terrane. In particular, rocks in this part of west-central Yukon appear to be stratigraphically correlative with, and share a similar structural style, deformation sequence, and metamorphic grade as the surrounding Permian to Early Jurassic metamorphic domain. However, the Australia Mountain domain records a transposition event associated with burial and metamorphism to 8–10 kbar and 650–680 °C in the Early to mid-Cretaceous (*c.* 146–118 Ma), which is not recorded in the surrounding Permian to Early Jurassic metamorphic domain. These observations require that the Australia Mountain domain occupied a deeper crustal level in the Early to mid-Cretaceous than the surrounding Permian to Early Jurassic metamorphic domain, and therefore provides a window into the Early to mid-Cretaceous infrastructure of the orogen in west-central Yukon. We apply the term 'infrastructure' in a similar sense to that suggested by De Sitter & Zwart (1960) and Culshaw *et al.* (2006) when describing mid- to lower-crustal levels in an orogen characterized by high-grade, shallowly dipping, ductily

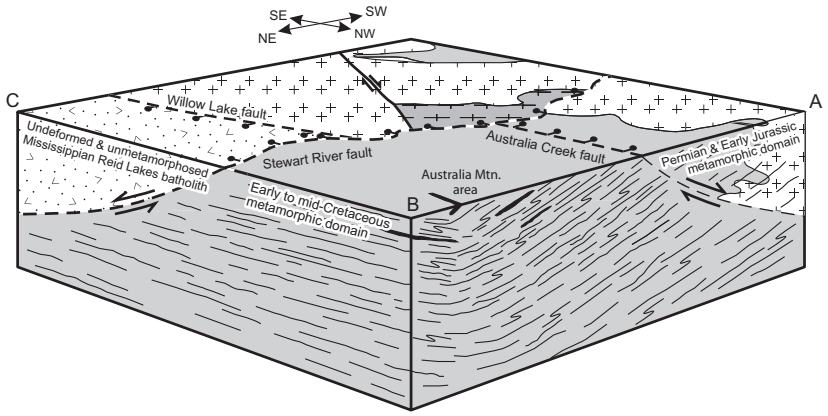

Figure 10. Schematic block diagram depicting the Cretaceous metamorphic domain (core complex?) at Australia Mountain, juxtaposed against the Mississippian Reid Lake plutonic complex and the Permian and Early Jurassic metamorphic domain by the Stewart River and Australia Creek faults. View is to the south. Location of cross-section lines indicated on Fig. 2. Fill patterns are in legend of Fig. 2.

deformed and transposed rocks. Conversely, the overlying 'superstructure' would be characterized by upright, brittle structures and low-metamorphic grade. For us, this rheological contrast between upper and lower crustal levels is time specific, in our case, the Early to mid-Cretaceous. We make this distinction because, as explained above, rocks formerly situated in the lower crust, the infrastructure, were progressively exhumed in the Jurassic and were incorporated into the superstructure above the Early to mid-Cretaceous infrastructure.

Our study indicates a pattern of structurally downward younging deformation and metamorphism in the Yukon-Tanana terrane, similar to what has been described in the southeastern Cordillera (Carr, 1991; Parrish, 1995; Crowley *et al.*, 2000; Gibson *et al.*, 2005). There, rocks buried, heated and exhumed in the Jurassic (Archibald *et al.*, 1983; Brown *et al.*, 1992; Colpron *et al.*, 1996; Gibson *et al.*, 2005), are now juxtaposed against structurally deeper rocks that were progressively buried and heated from Cretaceous to earliest Eocene (Brown & Carr, 1990; Carr, 1991; Parrish, 1995; Gibson *et al.*, 1999, 2005; Crowley & Parrish, 1999; Crowley *et al.*, 2000). Parrish (1995), Brown (2004) and Gibson *et al.* (2008) have all attributed this downward younging tectonism in the southeastern Canadian Cordillera to the progressive incorporation and burial of material as the burgeoning orogen propagated northeastward towards the foreland.

Monazite from this study dated at *c.* 112 Ma records the terminus of metamorphism and onset of near isothermal decompression and exhumation of deep seated metamorphic rocks of the Australia Mountain domain. Exhumation of this domain in the mid-Cretaceous is substantiated by the presence of metamorphic detritus (quartz with undulatory extinction, and lesser amounts of muscovite, feldspar and foliated lithic fragments) in the mid-Cretaceous (Albian) Indian River Formation (Lowey & Hills, 1988), ~35 km to the west. An isothermal decompression path alone may not be sufficient to distinguish between normal faulting and erosion as the dominant mechanism of exhumation (Ring *et al.*, 1999). However, the abrupt juxtaposition of the Cretaceous metamorphic domain at Australia Mountain against rocks with Early to Middle Jurassic cooling ages (Hunt & Roddick, 1992) strongly suggests the Australia Mountain domain is bound on its west side by a mid-Cretaceous normal fault, herein named the Australia Creek fault (Figs 2 & 10). Likewise, the juxtaposition of the Australia Mountain domain to the southeast against largely undeformed and unmetamorphosed rocks of the Mississippian Reid Lakes complex is interpreted to have been accommodated along a normal fault, herein named the Stewart River fault (Figs 2 & 10). Both of these faults are interpreted to have accommodated a significant amount of extensional exhumation in the mid-Cretaceous. Unfortunately, poor exposure in the area of the proposed faults has prevented the identification of corroborating deformation fabrics. Rather, the position of the fault is constrained by the jump in thermochronometric ages, the presence of a distinct discontinuity in aeromagnetic data for this region (Hayward *et al.*, 2012), and differences in lithologies (Permian Klondike schist present on west side of fault, abundant pre-late Devonian marble unit east of the fault).

Some 100 km to the west of Australia Mountain, rocks in east-central Alaska also record a shift to extensional tectonics in the mid-Cretaceous. The majority of metamorphic rocks in east-central Alaska are parautochthonous North American continental margin rocks with top-down-to-the-southeast shear fabrics and mid-Cretaceous cooling ages (Pavlis *et al.*, 1993; Hansen & Dusel-Bacon, 1998; Dusel-Bacon *et al.*, 2002). These amphibolite facies rocks with mid-Cretaceous $^{40}Ar/^{39}Ar$ and K-Ar cooling ages are juxtaposed across mylonitic shear zones against greenschist to amphibolite facies allochthonous rocks of Yukon-Tanana terrane with Early Jurassic cooling ages. Hansen & Dusel-Bacon (1998) and Dusel-Bacon *et al.* (2002) interpreted the top-down-to-the-southeast mylonitic shear zones to have formed during exhumation of the parautochthonous rocks from beneath the structurally overlying allochthonous Yukon-Tanana terrane.

The Cretaceous metamorphic domain in the Australia Mountain area likewise represents a window through a Cretaceous superstructure, with a Palaeozoic to Jurassic metamorphic and deformational history, revealing a much younger amphibolite facies Cretaceous infrastructure. Late Devonian (*c*. 363 Ma, Mortensen, 1990) and Early Mississippian (*c*. 348 Ma, Ruks *et al*., 2006) U-Pb ages from the Mount Burnham orthogneiss within the Australia Mountain domain are consistent with igneous activity known in both parautochthonous North American margin rocks and allochthonous Yukon-Tanana terrane in east-central Alaska as described by Dusel-Bacon *et al*. (2006). However, if the Australia Mountain domain is of parautochthonous North American continental margin affinity, then the Australia Creek fault represents a major terrane bounding extensional fault analogous to coeval mid-Cretaceous extensional faults described by Hansen & Dusel-Bacon (1998) and Dusel-Bacon *et al*. (2002) in east-central Alaska. Exhumation of structurally deep parautochthonous continental rocks from beneath the structurally overlying Yukon-Tanana terrane is highly conceivable considering that 25–30 km of crustal section (equivalent to the 9 kbar stage-2 peak metamorphic estimate) was removed in the middle Cretaceous following an earlier episode of exhumation of the Yukon-Tanana terrane in the Early Jurassic.

The Cretaceous domains at Australia Mountain and in east-central Alaska may be akin to the extensional core complexes identified throughout the North American Cordillera (Coney, 1980; Armstrong, 1982; Coney & Harms, 1984; Parrish *et al*., 1988; Struik, 1993), both in style and geological process. However, Cretaceous extensional exhumation in the northern Cordillera is distinctly older than the Eocene extension recorded in core complexes in the southern Canadian Cordillera and northwestern US (Parrish *et al*., 1988), and the Oligocene-Miocene extension in southwestern US (Coney, 1980).

CONCLUSIONS

Garnet growth zoning patterns within compositionally distinct inclusion-rich core and inclusion-poor rim domains, separated by an abrupt chemical discontinuity, are interpreted with the aid of modelled compositional and molar isopleths to record a two-stage garnet growth history, each reflective of a distinct metamorphic event. The early stages of growth of the inclusion-rich, stage-1 core (Grt-1) is interpreted to have initiated at conditions of ~600 °C, 8 kbar along a clockwise *P–T* path synchronous with the development of the external composite transposition foliation (S_T). Due to an absence of monazite inclusions within stage-1 garnet cores, this event remains undated. Growth of the relatively grossular-rich, pyrope-poor stage-2 overgrowth (Grt-2) is interpreted to have initiated at higher pressure, and/or lower temperature, than Grt-1, culminating at near-thermal peak *P–T* conditions of ~650–680 °C and 9 kbar. These peak thermobarometric estimates calculated from the composition of the rim of post-kinematic stage-2 garnet overgrowths (Grt-2) are consistent with the presence of syn- to post-kinematic kyanite, and require only minimal reaction overstepping (<20 °C) to explain the presence of syn- to post-kinematic staurolite. *In situ* U-Th-Pb SHRIMP dating of elongate monazite aligned with S_T in the matrix, and monazite included in syn- to post-kinematic, stage-2 porphyroblasts of staurolite and kyanite yield a single age population *c*. 117.5 ± 0.9 Ma. This age is interpreted to date the waning development of a reworked composite transposition foliation during stage-2 prograde metamorphism. These data, together with the data from Berman *et al*. (2007a), record a *c*. 146–118 Ma, 9 kbar amphibolite facies metamorphic and deformational event in the Australia Mountain area of west-central Yukon. However, contrary to the interpretation of Berman *et al*. (2007a), the younger mid-Cretaceous monazite ages (*c*. 112 Ma, this study; 114–107 Ma, Berman *et al*., 2007a) are not interpreted to date a distinct low-*P* contact metamorphic event. Rather, the presence of consistently young, Y-rich monazite, intimately associated with retrograde staurolite and plagioclase within resorbed portions of garnet, is interpreted to date the timing of garnet breakdown during decompression from the peak of metamorphism following the stage-2 garnet growth event. The results presented above indicate that in contrast to the majority of the Yukon-Tanana terrane, which was deformed and metamorphosed in the Permo-Triassic and exhumed to upper crustal levels in the Jurassic, the Australia Mountain domain occupied a deep crustal level (~25–30 km) in the Early to mid-Cretaceous. This area therefore represents a tectonic window into Early to mid Cretaceous infrastructure of the Yukon-Tanana terrane, potentially comparable to parautochthonous North American continental margin rocks beneath the Yukon-Tanana terrane in east-central Alaska, and may be akin to, but older than, extensional core complexes identified throughout the North American Cordillera.

ACKNOWLEDGEMENTS

This work was funded by NSERC grants to MC and DG, and NSERC scholarship to RS. Additional support was provided through the Geological Survey of Canada's (GSC) Geomapping for Energy and Minerals Program (GSC contribution # 20130035). We thank: P. Hunt at the GSC Ottawa for SEM imaging; M. Raudsepp and E. Czech at the University of British Columbia for assistance with microprobe analyses; and M. Jercinovic and the UMass microprobe lab for assistance with X-ray mapping of monazite. D. Tinkham is thanked for providing the thermodynamic data set tcds55 formatted for use with Theriak-Domino. N. Rayner, B. Davis and T. Pestaj at the Geological Survey of Canada SHRIMP

lab are thanked for assistance in the acquisition and reduction of the U-Th-Pb SHRIMP data. The manuscript benefited from discussions with D. Murphy, J. Mortensen and E. Knight. Constructive reviews by J. Mezger and C. Dusel-Bacon, and editorial handling by D. Robinson are gratefully acknowledged.

REFERENCES

Aranovich, L.Ya, 1991. *Mineral Equilibria of Multicomponent Solid Solutions*. Nauka Press, Moscow.

Archibald, D.A., Glover, J.K., Price, R.A., Farrar, E. & Carmichael, D.M., 1983. Geochronology and tectonic implications of magmatism and metamorphism, southern Kootenay Arc and neighbouring regions, southeastern British Columbia. Part I: Jurassic to mid-Cretaceous. *Canadian Journal of Earth Sciences*, **20,** 1891–1913.

Armstrong, R.L., 1982. Cordilleran metamorphic core complexes–from Arizona to southern Canada. *Annual Review of Earth and Planetary Science Letters*, **10,** 129–154.

Ashworth, J.R. & Evirgen, M.M., 1985. Plagioclase relations in pelites, central Menderes Massif, Turkey. II. Perturbation of garnet-plagioclase geobarometers. *Journal of Metamorphic Geology*, **3,** 219–229.

Bea, F. & Montero, P., 1999. Behavior of accessory phases and redistribution of Zr, REE, Y, Th, and U during metamorphism and partial melting of metapelites in the lower crust: an example from the Kinzigite Formation of Ivrea–Verbano, NW Italy. *Geochimica et Cosmochimica Acta*, **63,** 1113–1153.

Beranek, L.P. & Mortensen, J.K., 2011. The timing and provenance record of the Late Permian Klondike orogeny in northwestern Canada and arc-continent collision along western North America. *Tectonics*, **30:** TC5017, doi:10.1029/2010TC002849.

Berman, R.G., 1991. Thermobarometry using multi-equilibrium calculations: a new technique, with petrological applications. *Canadian Mineralogist*, **29,** 833–855.

Berman, R.G. 2007. winTWQ (version 2.3): A Microsoft Windows-compatible software package for performing internally-consistent thermobarometric calculations. Geological Survey of Canada Open File, 5462.

Berman, R., Sanborn-Barrie, M., Stern, R. & Carson, C., 2005. Tectonometamorphism at c. 2.35 and 1.85 Ga in the Rae domain, western Churchill Province, Nunavut, Canada: insights from structural, metamorphic and *in situ* geochronological analysis of the southwestern Committee Bay belt. *Canadian Mineralogist*, **43,** 409–442.

Berman, R.G., Ryan, J.J., Gordey, S.P. & Villeneuve, M., 2007a. Permian to Cretaceous polymetamorphic evolution of the Stewart River region, Yukon-Tanana terrane, Yukon, Canada: P-T evolution linked with in-situ SHRIMP monazite geochronology. *Journal of Metamorphic Geology*, **25,** 803–827.

Berman, R.G., Aranovich, L.Y., Rancourt, D.G. & Mercier, P.H.J., 2007b. Reversed phase equilibrium constraints on the stability of Mg-Fe-Al biotite. *American Mineralogist*, **92,** 139–150.

Berman, R.G., Sanborn-Barrie, M., Rayner, N., Carson, C., Sandeman, H.A. & Skulski, T., 2010. Petrological and *in situ* SHRIMP geochronological constraints on the tectonometamorphic evolution of the Committee Bay belt, Rae Province, Nunavut. *Precambrian Research*, **181,** 1–20.

Berman, R.G., Rayner, N., Sanborn-Barrie, M. & Whalen, J. (in press). The tectonometamorphic evolution of Southampton Island, Nunavut: insight from petrologic modeling and in situ SHRIMP geochronology of multiple episodes of monazite growth. *Precambrian Research*.

Braun, I., Montel, J.M. & Nicollet, C., 1998. Electron microprobe dating of monazites from high-grade gneisses and pegmatites of the Kerala Khondalite Belt, southern India. *Chemical Geology*, **146,** 65–85.

Brown, R.L., 2004. Thrust-belt accretion and hinterland underplating of orogenic wedges: an example from the Canadian Cordillera. In: *Thrust Tectonics and Hydrocarbon Systems* (ed. McClay, K.R.), *American Association of Petroleum Geologists (AAPG) Memoir* **82,** 51–64.

Brown, R.L. & Carr, S.D., 1990. Lithospheric thickening and orogenic collapse within the Canadian Cordillera. *Proceedings of the Pacific Rim 90 Congress, Australian Institute of Mining and Metallogeny*, **2,** 1–10.

Brown, R.L., McNicoll, V.J., Parrish, R.R. & Scammell, R.J., 1992. Middle Jurassic plutonism in the Kootenay Terrane, northern Selkirk Mountains, British Columbia. In: *Radiogenic Age and Isotopic Studies: Report 5*. Geological Survey of Canada, Paper 91-2, pp. 135–141.

Brown, S.R., Gibson, H.D., Andrews, G.D.M. *et al.*, 2012. New constraints on Eocene extension within the Canadian Cordillera and identification of Phanerozoic protoliths for footwall gneisses of the Okanagan Valley shear zone. *Lithosphere*, **4,** 354–377.

Caddick, M.J., Bickle, M.J., Harris, N.B.W., Holland, T.J.B., Horstwood, M.S.A. & Ahmad, T., 2007. Burial and exhumation history of a Lesser Himalayan schist: recording the formation of an inverted metamorphic sequence in NW India. *Earth and Planetary Science Letters*, **264,** 375–390.

Carr, S.D., 1991. Three crustal zones in the Thor-Odin-Pinnacles area, southern Omineca belt, British Columbia. *Canadian Journal of Earth Sciences*, **28,** 2003–2023.

Chatterjee, N.D. & Froese, E., 1975. A thermodynamic study of the pseudobinary join muscovite-paragonite in the system $KAlSi_3O_8$–$NaAlSi_3O_8$-Al_2O_3-SiO_2-H_2O. *American Mineralogist*, **60,** 985–993.

Cheng, H., Vervoort, J.D., Li, X., Zhang, C., Li, Q. & Zheng, S., 2011. The growth interval of garnet in the UHP eclogites from the Dabie orogen, China. *American Mineralogist*, **96,** 1300–1307.

Cherniak, D.J., Watson, E.B., Grove, M. & Harrison, T.M., 2004. Pb diffusion in monazite: a combined RBS/SIMS study. *Geochimica et Cosmochimica Acta*, **68,** 829–840.

Cocherie, A., Legendre, O., Peucat, J.J. & Kouamelan, A.N., 1998. Geochronology of polygenetic monazites constrained by *in situ* electron-microprobe Th–U total lead determination–implications for lead behavior in monazite. *Geochimica et Cosmochimica Acta*, **62,** 2475–2497.

Coggon, R. & Holland, T.J.B., 2002. Mixing properties of phengitic micas and revised garnet-phengite thermobarometers. *Journal of Metamorphic Geology*, **20,** 683–696.

Colpron, M. & Ryan, J.J., 2010. Bedrock geology of southwest McQuesten (NTS 115P) and part of northern Carmacks (NTS 115I) map area. In: *Yukon Exploration and Geology 2009* (eds MacFarlane, K.E., Weston, L.H. & Blackburn, L.R.), pp. 159–184. Yukon Geological Survey, Whitehorse, Yukon.

Colpron, M., Price, R.A., Archibald, D.A. & Carmichael, D.M., 1996. Middle Jurassic exhumation along the western flank of the Selkirk fan structure: thermobarometric and thermochronometric constraints from the Illecillewaet synclinorium, southeastern British Columbia. *Geological Society of America Bulletin*, **108,** 1372–1392.

Colpron, M., Nelson, J.L. & Murphy, D.C., 2006. A tectonostratigraphic framework for the pericratonic terranes of the northern Canadian Cordillera. In: *Paleozoic Evolution and Metallogeny of Pericratonic Terranes at the Ancient Pacific Margin of North America, Canadian and Alaskan Cordillera, Special Paper 45* (eds Colpron, M. & Nelson, J.L.), pp. 1–23. Geological Association of Canada, St. John's, Newfoundland.

Colpron, M., Nelson, J.L. & Murphy, D.C., 2007. Northern Cordilleran terranes and their interactions through time. *GSA Today*, **17,** 4–10.

Coney, P.J., 1980. Cordilleran core complexes; an overview. In: *Cordilleran Metamorphic Core Complexes, Memoir 153* (eds Crittenden, M.D., Coney, P.J. & Davis, G.H.), pp. 7–34. Geological Society of America, Boulder, CO.

Coney, P.J. & Harms, T.A., 1984. Cordilleran metamorphic core complexes: Cenozoic extensional relics of Mesozoic compression. *Geology*, **12,** 550–554.

Crowley, J.L. & Ghent, E.D., 1999. An electron microprobe study of the U-Th-Pb systematics of metamorphosed monazite: the role of Pb diffusion versus overgrowth and recrystallization. *Chemical Geology*, **157,** 285–302.

Crowley, J.L. & Parrish, R.R., 1999. U-Pb isotopic constraints on diachronous metamorphism in the northern Monashee complex, southern Canadian Cordillera. *Journal of Metamorphic Geology*, **17,** 483–502.

Crowley, J.L., Ghent, E.D., Carr, S.D., Simony, P.S. & Hamilton, M.A., 2000. Multiple thermotectonic events in a continuous metamorphic sequence, Mica Creek area, southeastern Canadian Cordillera. *Geological Materials Research*, **2,** 1–45.

Culshaw, N.G., Beaumont, C. & Jamieson, R.A., 2006. The orogenic superstructure-infrastructure concept: revisited, quantified, and revived. *Geology*, **34,** 733–736.

De Capitani, C. & Brown, T.H., 1987. The computation of chemical equilibrium in complex systems containing non-ideal solutions. *Geochimica et Cosmochimica Acta*, **51,** 2639–2652.

De Capitani, C. & Petrakakis, K., 2010. The computation of equilibrium assemblage diagrams with Theriak/Domino software. *American Mineralogist*, **95,** 1006–1016.

De Sitter, L.U. & Zwart, H.J., 1960. Tectonic development in supra- and infra-structures of a mountain chain. *21st International Geological Congress, Copenhagen*, **18,** 249–256.

DeWolf, C.P., Belshaw, N. & O'Nions, R.K., 1993. A metamorphic history from micron-scale $^{207}Pb/^{206}Pb$ chronometry of Archean monazite. *Earth and Planetary Science Letters*, **120,** 207–220.

Dusel-Bacon, C., Hansen, V.L. & Scala, J.A., 1995. High-pressure amphibolite facies dynamic metamorphism and the Mesozoic tectonic evolution of an ancient continental margin, east-central Alaska. *Journal of Metamorphic Geology*, **13,** 9–24.

Dusel-Bacon, C., Lanphere, M.A., Sharp, W.D., Layer, P.W. & Hansen, V.L., 2002. Mesozoic thermal history and timing of structural events for the Yukon-Tanana Upland, east-central Alaska: $^{40}Ar/^{39}Ar$ data from metamorphic and plutonic rocks. *Canadian Journal of Earth Sciences*, **39,** 1013–1051.

Dusel-Bacon, C., Hopkins, M.J., Mortensen, J.K., Dashevsky, S.S., Bressler, J.R. & Day, W.C., 2006. Paleozoic tectonic and metallogenic evolution of the pericratonic rocks of east-central Alaska and adjacent Yukon. In: *Paleozoic Evolution and Metallogeny of Pericratonic Terranes at the Ancient Pacific Margin of North America, Canadian and Alaskan Cordillera, Special Paper 45* (eds Colpron, M. & Nelson, J.L.), pp. 1–23. Geological Association of Canada, St. John's, Newfoundland.

Fitzsimons, I.C.W., Kinny, P.D., Wetherley, S. & Hollingsworth, D.A., 2005. Bulk chemical control on metamorphic monazite growth in pelitic schists and implications for U-Pb age data. *Journal of Metamorphic Geology*, **23,** 261–277.

Florence, F.P. & Spear, F.S., 1993. Influences of reaction history and chemical diffusion on P-T calculations for staurolite schists from the Littleton Formation, northwestern New Hampshire. *American Mineralogist*, **78,** 345–359.

Foster, G., Gibson, H.D., Parrish, R.R., Horstwood, M., Fraser, J. & Tindle, A., 2002. Textural, chemical and isotopic insights into the nature and behaviour of metamorphic monazite. *Chemical Geology*, **191,** 183–207.

Foster, G., Parrish, R.R., Horstwood, M.S.A., Chenery, S., Pyle, J. & Gibson, H.D., 2004. The generation of prograde P-T–t points and paths; a textural, compositional, and chronological study of metamorphic monazite. *Earth Planetary Science Letters*, **228,** 125–142.

Fuhrman, M.L. & Lindsley, D.H., 1988. Ternary-feldspar modeling and thermometry. *American Mineralogist*, **73,** 201–216.

Gabrielse, H., Murphy, D.C. & Mortensen, J.K., 2006. Cretaceous and Cenozoic dextral orogen-parallel displacements, magmatism and paleogeography, north-central Canadian Cordillera. In: *Paleogeography of the North American Cordillera: Evidence for and Against Large-Scale Displacements, Special Paper 46* (eds Haggart, J.W., Monger, J.W.H. & Enkin, R.J.), pp. 255–276. Geological Association of Canada, St. John's, Newfoundland.

Gaidies, F., Krenn, E., de Capitani, C. & Abart, R., 2008. Coupling forward modelling of garnet growth with monazite geochronology: an application to the Rappold complex (Austroalpine crystalline basement). *Journal of Metamorphic Geology*, **26,** 775–793.

Gardés, E., Jaoul, O., Montel, J.-M., Seydoux-Guillaume, A.-M. & Wirth, R., 2006. Pb diffusion in monazite: an experimental study of $Pb^{2+} + Th^{4+} \Leftrightarrow 2Nd^{3+}$ interdiffusion. *Geochimica et Cosmochimica Acta*, **70,** 2325–2336.

Gibson, H.D., Brown, R.L. & Parrish, R.R., 1999. Deformation-induced inverted metamorphic field gradients: an example from the southeastern Canadian Cordillera. *Journal of Structural Geology*, **21,** 751–767.

Gibson, H.D., Carr, S.D., Brown, R.L. & Hamilton, M.A., 2004. Correlations between chemical and age domains in monazite, and metamorphic reactions involving major politic phases: an integration of ID-TIMS and SHRIMP geochronology with Y-Th–U X-ray mapping. *Chemical Geology*, **211,** 237–260.

Gibson, H.D., Brown, R.L. & Carr, S.D., 2005. U-Th- Pb geochronologic constraints on the structural evolution of the Selkirk fan, northern Selkirk Mountains, southern Canadian Cordillera. *Journal of Structural Geology*, **27,** 1899–1924.

Gibson, H.D., Brown, R.L. & Carr, S.D., 2008. Tectonic evolution of the Selkirk fan, southeastern Canadian Cordillera: a composite Middle Jurassic–Cretaceous orogenic structure. *Tectonics*, **27,** TC6007, doi: 10.1029/2007TC002160.

Goncalves, P., Williams, M.L. & Jercinovic, M.J., 2005. Electron-microprobe age mapping of monazite. *American Mineralogist*, **90,** 578–585.

Gordey, S.P. & Ryan, J.J., 2005. Geology, Stewart River area (115N, 115-O and part of 115J), Yukon Territory. Geological Survey of Canada, Open File 4970 (1 sheet, 1:250 000 scale).

Hansen, V.L. & Dusel-Bacon, C., 1998. Structural and Kinematic evolution of the Yukon-Tanana upland tectonites, east-central Alaska: a record of late Paleozoic to Mesozoic crustal assembly. *Geological Society of America Bulletin*, **110,** 211–230.

Hansen, V.L., Heizler, M.T. & Harrison, T.M., 1991. Mesozoic thermal evolution of the Yukon-Tanana composite terrane; new evidence from $^{40}Ar/^{39}Ar$ data. *Tectonics*, **10,** 51–76.

Harlov, D.E. & Hetherington, C.J., 2010. Partial high-grade alteration of monazite using alkali-bearing fluids: experiment and nature. *American Mineralogist*, **95,** 1105–1108.

Harlov, D.E., Wirth, R. & Hetherington, C.J., 2011. Fluid-mediated partial alteration in monazite: the role of coupled dissolution–reprecipitation in element redistribution and mass transfer. *Contributions to Mineralogy and Petrology*, **162,** 329–348.

Hayward, N., Miles, W. & Oneschuk, D. 2012. Geophysical Series, detailed geophysical compilation project, Yukon Plateau, Yukon, NTS 115-I, J, K, N, O, P and 116A and B. Geological Survey of Canada, Open File 7279 (2 sheets, 1:350 000 Scale).

Hetherington, C.J., Harlov, D.E. & Budzyń, B., 2010. Experimental metasomatism of monazite and xenotime: mineral stability, REE mobility and fluid composition. *Mineralogy and Petrology*, **99,** 165–184.

Holland, T.J.B. & Powell, R., 1998. An internally consistent thermodynamic data set for phases of petrological interest. *Journal of Metamorphic Geology*, **16,** 309–343.

Holland, T. & Powell, R., 2003. Activity-composition relations for phases in petrological calculations; an asymmetric multicomponent formulation. *Contributions to Mineralogy and Petrology*, **145,** 492–501.

Horváth, P., Balen, D., Finger, F., Tomljenović, B. & Krenn, E., 2010. Contrasting P-T–t paths from the basement of the Tisia Unit (Slavonian Mts., NE Croatia): application of quantitative phase diagrams and monazite age dating. *Lithos*, **117,** 269–282.

Hunt, P.A. & Roddick, J.C., 1992. A compilation of K–Ar and ^{40}Ar–^{39}Ar ages: report 22. In: *Radiogenic Age and Isotopic Studies: Report 6*. Geological Survey of Canada, Paper 92-2, pp. 179–226.

Ireland, T.R. & Gibson, G.M., 1998. SHRIMP monazite and zircon geochronology of high-grade metamorphism in New Zealand. *Journal of Metamorphic Geology*, **16,** 149–167.

Janots, E., Engi, M., Berger, A., Allaz, J., Schwarz, J.O. & Spandler, C., 2008. Prograde metamorphic sequence of REE minerals in pelitic rocks of the Central Alps, implications for allanite–monazite–xenotime phase relations from 250 to 610 °C. *Journal of Metamorphic Geology*, **26,** 509–526.

Johnston, S.T., Mortensen, J.K. & Erdmer, P., 1996. Igneous and metaigneous age constraints for the Aishihik metamorphic suite, southwest Yukon. *Canadian Journal of Earth Sciences*, **33,** 1543–1555.

Knight, E., Schneider, D.A. & Ryan, J.J., 2013. Thermochronology of the Yukon-Tanana terrane, west-central Yukon: evidence for Jurassic extension and exhumation in the northern Canadian Cordillera. *Journal of Geology*, **121,** 371–400

Kohn, M.J. & Spear, F., 2000. Retrograde net transfer reaction insurance for pressure-temperature estimates. *Geology*, **28,** 1127–1130.

Kretz, R., 1983. Symbols for rock-forming minerals. *American Mineralogist*, **68,** 277–279.

Lowey, G.W. & Hills, L.V., 1988. Lithofacies, petrography, and environments of deposition, Tantalus Formation (Lower Cretaceous), Indian River area, west-central Yukon. *Bulletin of Canadian Petroleum Geology*, **36,** 296–310.

Ludwig, K.R., 2008. *Manual for Isoplot 3.7: A Geochronological Toolkit for Microsoft Excel*. Special Publication No. 4. rev. August 26, 2008, Berkeley Geochronology Center, Berkeley, CA, 77pp.

Mackenzie, D. & Craw, D., 2012. Contrasting structural settings of mafic and ultramafic rocks in the Yukon-Tanana terrane. In: *Yukon Exploration and Geology 2011* (eds MacFarlane, K.E. & Sack, P.J.), pp. 115–127. Yukon Geological Survey, Whitehorse, Yukon.

Mattison, C.G., Wooden, J.L., Liou, J.G., Bird, D.K. & Wu, C.L., 2006. Age and duration of eclogite-facies metamorphism, north Qaidam HP/UHP terrane, western China. *American Journal of Science*, **306,** 683–711.

Monger, J.W.H. & Price, R.A., 2002. The Canadian Cordillera: geology and tectonic evolution. *Canadian Society of Exploration Geophysicists Recorder*, **27,** 17–36.

Monger, J.W.H., Price, R.A. & Tempelman-Kluit, D.J., 1982. Tectonic accretion and the origin of the two major metamorphic and plutonic welts in the Canadian Cordillera. *Geology*, **10,** 70–75.

Mortensen, J.K., 1990. Geology and U-Pb geochronology of the Klondike District, west-central Yukon Territory. *Canadian Journal of Earth Sciences*, **27,** 903–914.

Murphy, D.C., 2004. Devonian-Mississippian metavolcanic stratigraphy, massive sulphide potential and structural re-interpretation of Yukon-Tanana Terrane south of the Finlayson Lake massive district, southeastern Yukon (105G/1, 105H/3,4,5). In: *Yukon Exploration and Geology 2003* (eds Emond, D.S. & Lewis, L.L.), pp. 157–175. Yukon Geological Survey, Whitehorse, Yukon.

Murphy, D.C., van der Heyden, P., Parrish, R.R. *et al*., 1995. New geochronological constraints on Jurassic deformation of the western edge of North America, southeastern Canadian Cordillera. In: *Jurassic Magmatism and Tectonics of the North American Cordillera, Special Paper 299* (eds Miller, D.M. & Busby, C.), pp. 159–171. Geological Society of America, Boulder, CO.

Nelson, J.L., Colpron, M., Piercey, S.J., Dusel-Bacon, C., Murphy, D.C. & Roots, C.F., 2006. Paleozoic tectonic and metallogenic evolution of the pericratonic terranes in Yukon, northern British Columbia and eastern Alaska. In: *Paleozoic Evolution and Metallogeny of Pericratonic Terranes at the Ancient Pacific Margin of North America, Canadian and Alaskan Cordillera, Special Paper 45* (eds Colpron, M. & Nelson, J.L.), pp. 323–360. Geological Association of Canada, St. John's, Newfoundland.

Parrish, R.R., 1995. Thermal evolution of the southeastern Canadian Cordillera. *Canadian Journal of Earth Sciences*, **32,** 1618–1642.

Parrish, R.R., Carr, S.D. & Parkinson, D.L., 1988. Eocene extensional tectonics and geochronology of the southern Omineca belt, British Columbia and Washington. *Tectonics*, **7,** 181–212.

Pattison, D.R.M. & Tinkham, D.T., 2009. Interplay between equilibrium and kinetics in prograde metamorphism of pelites: an example from the Nelson aureole, British Columbia. *Journal of Metamorphic Geology*, **27,** 249–279.

Pattison, D.R.M., de Capitani, C. & Gaidies, F., 2011. Petrological consequences of variations in metamorphic reaction history. *Journal of Metamorphic Geology*, **29,** 953–977.

Pavlis, T.L., Sisson, V.B., Foster, H.L., Nockleberg, W.J. & Plafker, G., 1993. Mid-Cretaceous extensional tectonics of the Yukon–Tanana terrane, Trans-Alaskan Crustal Transect (TACT), east-central Alaska. *Tectonics*, **12,** 103–122.

Pyle, J.M. & Spear, F.S., 1999. Yttrium zoning in garnet: coupling of major and accessory phases during metamorphic reactions. *Geological Materials Research*, **1,** 1–49.

Rayner, N. & Stern, R.A., 2002. *Improved Sample Preparation Method for SHRIMP Analysis of Delicate Mineral Grains Exposed in Thin Sections*. Geological Survey of Canada, Current Research 2002-F10, 1–3.

Ring, U., Brandon, M.T., Willet, S.D. & Lister, G.S., 1999. Exhumation processes. In: *Exhumation Processes: Normal Faulting, Ductile Flow, and Erosion* (eds Ring, U., Brandon, M.T., Lister, G.S. & Willet, S.D.), pp. 1–27. Geological Society of London, Special Publications.

Ruks, T.W., Piercey, S.J., Ryan, J.J., Villeneuve, M.E. & Creaser, R.A., 2006. Mid- to Late Paleozoic K-feldspar augen granitoids of the Yukon-Tanana terrane, Yukon: implications for crustal growth and tectonic evolution of the northern Cordillera. *Geological Society of America Bulletin*, **118,** 1212–1231.

Ryan, J.J., Gordey, S.P., Glombick, P., Piercey, S.J. & Villeneuve, M.E., 2003. *Update on Bedrock Geological Mapping of the Yukon-Tanana Terrane, Southern Stewart River Map Area, Yukon Territory*. Geological Survey of Canada, Current Research 2003-A9. 7p.

Ryan, J.J., Colpron, M. & Hayward, N., 2010. Geology, southwestern McQuesten and parts of northern Carmacks, Yukon; Geological Survey of Canada, Canadian Geoscience Map 7, (preliminary version), scale 1:125 000.

Schärer, U., 1984. The effect of initial ^{230}Th disequilibrium on young U-Pb ages: the Makalu case, Himalaya. *Earth and Planetary Science Letters*, **67,** 191–204.

Seydoux-Guillaume, A.M., Paquette, J.L., Wiedenbeck, M., Montel, J.-M. & Heinrich, W., 2002. Experimental resetting of the U-Th–Pb systems in monazite. *Chemical Geology*, **191,** 165–181.

Skora, S., Lapen, T.J., Baumgartner, L.P., Johnson, C.M., Hellebrand, E. & Mahlen, M.J., 2009. The duration of prograde garnet crystallization in the UHP eclogites at Lago di Cignana, Italy. *Earth and Planetary Science Letters*, **287,** 402–411.

Spear, F.S. & Parrish, R.R., 1996. Petrology and cooling rates of the Valhalla complex, British Columbia, Canada. *Journal of Petrology*, **37,** 733–765.

Spear, F.S., Kohn, M.J., Florence, F.P. & Menard, T., 1990. A model for garnet and plagioclase growth in pelitic schists: implications for thermobarometry and *P-T* path determinations. *Journal of Metamorphic Geology*, **8,** 683–696.

Stacey, J.S. & Kramers, J.D., 1975. Approximation of terrestrial lead isotope evolution by a two-stage model. *Earth and Planetary Science Letters*, **26,** 207–221.

Stern, R.A., 1997. The GSC sensitive high resolution ion microphobe (SHRIMP): analytical techniques of zircon U-Th-Pb age determinations and performance evaluation. *Radiogenic Age and Isotopic Studies: Report 10*. Geological Survey of Canada, Current Research 1997-F, 1–31.

Stern, R.A. & Berman, R.G., 2000. Monazite U-Pb and Th-Pb geochronology by ion microprobe, with an application to *in situ* dating of an Archean metasedimentary rock. *Chemical Geology*, **172,** 113–130.

Stern, R.A. & Sanborn, N., 1998. Monazite U–Pb and Th–Pb geochronology by high-resolution secondary ion mass spectrometry. *Radiogenic Age and Isotopic Studies: Report 11*. Geological Survey of Canada, Current Research 1998-F. 1–18.

Stevens, R.A., Mortensen, J.K. & Hunt, P.A., 1993. U–Pb and 40Ar/39Ar geochronology of plutonic rocks from the Teslin suture zone, Yukon Territory. In: *Radiogenic and Isotope Studies, Report 7*. Geological Survey of Canada, Paper 93-2, pp. 83–90.

Struik, L.C., 1993. Intersecting intracontinental Tertiary transform fault systems in the North American Cordillera. *Canadian Journal of Earth Sciences*, **30,** 1262–1274.

Stüwe, K., 1997. Effective bulk composition changes due to cooling: a model predicting complexities in retrograde reaction textures. *Contributions to Mineralogy and Petrology*, **129,** 43–52.

Tinkham, D.K., Zuluaga, C.A. & Stowell, H.H., 2001. Metapelite phase equilibria modeling in MnNCKFMASH: the effect of variable Al_2O_3 and MgO/(MgO+FeO) on mineral stability. *Geological Materials Research*, **3,** 1–42.

Tobisch, O.T. & Paterson, S.C., 1988. Analysis and interpretation of composite foliations in an area of progressive deformation. *Journal of Structural Geology*, **10,** 745–754.

Todd, C., 1998. Limits on the precision of geobarometry at low grossular and anorthite content. *American Mineralogist*, **83,** 1161–1167.

Tracy, R.J., Robinson, P. & Thompson, A.B., 1976. Garnet composition and zoning in the determination of temperature and pressure of metamorphism, central Massachusetts. *American Mineralogist*, **61,** 762–775.

Vance, D. & Mahar, E., 1998. Pressure–temperature paths from P-T pseudosections and zoned garnets; potential, limitations and examples from the Zanskar Himalaya, NW India. *Contributions to Mineralogy and Petrology*, **132,** 225–245.

Waters, D.J. & Lovegrove, D.P., 2002. Assessing the extent of disequilibrium and overstepping of prograde metamorphic reactions in metapelites from the Bushveld Complex aureole, South Africa. *Journal of Metamorphic Geology*, **20,** 135–149.

White, R.W., Powell, R., Holland, T.J.B. & Worley, B.A., 2000. The effect of TiO_2 and Fe_2O_3 on metapelitic assemblages at greenschist and amphibolite facies conditions: mineral equilibria calculations in the system K_2O–FeO–MgO–Al_2O_3–SiO_2–H_2O–TiO_2–Fe_2O_3. *Journal of Metamorphic Geology*, **18,** 497–511.

White, R.W., Powell, R. & Holland, T.J.B., 2007. Progress relating to calculations of partial melting equilibria for metapelites. *Journal of Metamorphic Geology*, **25,** 511–527.

Williams, P.F., 1983. Large scale transposition by folding in Northern Norway. *Geologische Rundschau*, **72,** 589–604.

Williams, P.F., 1985. Multiply deformed terrains-problems of correlation. *Journal of Structural Geology*, **7,** 269–280.

Williams, P.F. & Compagnoni, R., 1983. Deformation and metamorphism in the Bard area of the Sesia Lanzo zone, Western Alps, during subduction and uplift. *Journal of Metamorphic Geology*, **1,** 117–140.

Williams, M.L. & Jercinovic, M.J., 2002. Microprobe monazite geochronology: putting absolute time into microstructural analysis. *Journal of Structural Geology*, **24,** 1013–1028.

Williams, M.L., Jercinovic, M.J. & Terry, M.P., 1999. Age mapping and dating of monazite on the electron microprobe: Deconvoluting multistage tectonic histories. *Geology*, **27,** 1023–1026.

Williams, M.L., Jercinovic, M.J., Harlov, D.E., Budzyń, B. & Hetherington, C.J., 2011. Resetting monazite ages during fluid-related alteration. *Chemical Geology*, **283,** 218–225.

Wolf, D.E., Andronicos, C.L., Vervoort, J.D., Mansfield, M.R. & Chardon, D., 2010. Application of Lu-Hf garnet dating to unravel the relationships between deformation, metamorphism and plutonism: an example from the Prince Rupert area, British Columbia. *Tectonophisics*, **485,** 62–77.

Zhu, X.K. & O'Nions, R.K., 1999. Zonation of monazite in metamorphic rocks and its implications for high temperature thermochronology: a case study from the Lewisian terrain. *Earth and Planetary Science Letters*, **171,** 209–220.

SUPPORTING INFORMATION

Additional Supporting Information may be found in the online version of this article at the publisher's web site:

Table S1. SHRIMP U-Th-Pb analytical data for monazite corrected using the ^{204}Pb-method.

Received 17 January 2013; revision accepted 24 May 2013.